CELLULAR NEUROSCIENCE

An asymmetric mechanical code ciphers curvature-dependent proprioceptor activity

Ravi Das[†], Li-Chun Lin[†], Frederic Català-Castro[†], Nawaphat Malaiwong[†], Neus Sanfeliu-Cerdán, Montserrat Porta-de-la-Riva, Aleksandra Pidde, Michael Krieg*

A repetitive gait cycle is an archetypical component within the behavioral repertoire of many animals including humans. It originates from mechanical feedback within proprioceptors to adjust the motor program during locomotion and thus leads to a periodic orbit in a low-dimensional space. Here, we investigate the mechanics, molecules, and neurons responsible for proprioception in Caenorhabditis elegans to gain insight into how mechanosensation shapes the orbital trajectory to a well-defined limit cycle. We used genome editing, force spectroscopy, and multiscale modeling and found that alternating tension and compression with the spectrin network of a single proprioceptor encodes body posture and informs TRP-4/NOMPC and TWK-16/TREK2 homologs of mechanosensitive ion channels during locomotion. In contrast to a widely accepted model of proprioceptive "stretch" reception, we found that proprioceptors activated locally under compressive stresses in-vivo and in-vitro and propose that this property leads to compartmentalized activity within long axons delimited by curvature-dependent mechanical stresses.

INTRODUCTION

Many, if not all, motile animals generate forward thrust that is powered by collective cell shape changes due to antagonizing muscle activity. In *Caenorhabditis elegans*, the associated contraction/relaxation cycles are performed with submaximal capacity and are driven by four classes of coupled excitatory and inhibitory motor neurons (*1*), giving rise to the tailward propagating wave that bends the body with a given curvature (*2*). The amplitude of these optimal driving patterns is robust against external and internal perturbations, due, in part, to mechanosensitive feedback from specialized sensory cells and neurons that signal the mechanical deformation to the central nervous system (*3*). Several proprioceptor neurons have been identified in *C. elegans* that become activated upon spontaneous or imposed body bending, such as DVA, PVD, SMD, and the motor circuit itself (*4–8*), all of which express mechanoelectrical transduction (MeT) channels that are likely candidates to read out the mechanical strains and stresses that arise during locomotion (*9*, *10*). However, we still have little knowledge about the physiologically relevant mechanical stresses and deformations that lead to the activation of mechanosensitive neurons during proprioception or visceral mechanosensation (*11*). This is due, in part, to the complexity of animal anatomy confounded by the coexistence of multiple MeT channels, their differential sensitivity to specific stress tensors (*12*, *13*), and the associated difficulty to record from the mechanosensor in moving specimens. Contrary to intuition, structure-guided modeling revealed that one of the best characterized MeT channels of the transient receptor potential (TRP) family, no mechanoreceptor potential C (NOMPC) (*14*, *15*), is gated under compressive stresses (*16*, *17*). In contrast, members of the ubiquitously expressed two-pore potassium (K2P) channels activate under mechanical tension (*18*). Because TRP and K2P channels have opposing roles on neuronal (de)polarization (*15*), strain selectivity of these ion channels could fine-tune neuronal responses in a dynamic environment (*19*).

ICFO, Institut de Ciències Fotòniques, Castelldefels, Spain.
*Corresponding author. Email: michael.krieg@icfo.eu
†These authors are the main contributors.

Here, we identify that DVA in *C. elegans* activates upon compressive stresses in the spectrin cytoskeleton in a NOMPC/TRP-4–dependent manner, while mechanical tension attenuates neuronal activity and prevents calcium signals through the K2P homolog TWK-16. We speculate that this mechanical interplay is particularly important during body movement to confine neuronal activity within controlled regions when positive and negative stresses coincide in long sensory neurites.

RESULTS

β-Spectrin curbs body bends

We previously identified UNC-70 β-spectrin, as a key cytoskeletal component that is under mechanical tension in neurons in *C. elegans* (*20*). We noticed that the same mutations that lead to a failure to detect forces during gentle body touch also increase body curvature during locomotion. Thus, we conjectured that UNC-70 might have roles in proprioception during locomotion and recorded short videos of freely moving wild-type (wt) and *unc-70* mutant animals. We found that wt animals moved in their stereotyped undulatory fashion, whereas *unc-70(e524)* animals consistently and invariantly moved with deeper body bends (Fig. 1, A and B, and movie S1). To obtain a more quantitative picture, we set up an image processing pipeline to extract the centerline of each body posture. We then used principal components analysis (see Materials and Methods and table S1 for details) to represent the emergent locomotion pattern as a periodic orbit in a low-dimensional space, using the modes (a_1, a_2, and a_3), which are derived using the eigenworms (Fig. 1, A and B) (*21*, *22*). In this formalism, the eigenworms span a parametric space for postural dynamics adopted by *C. elegans* as it crawls, such that behavior can be plotted and compared within a simple three-dimensional (3D) Cartesian coordinate system. The first two modes (a_1 and a_2) describe the forward locomotion. The third mode has been attributed to turning behavior and deep body bends (*21*, *23*).

Trajectories derived from wt animals form a phase-locked orbit, with a limit corresponding to the amplitude of the body bends, but,
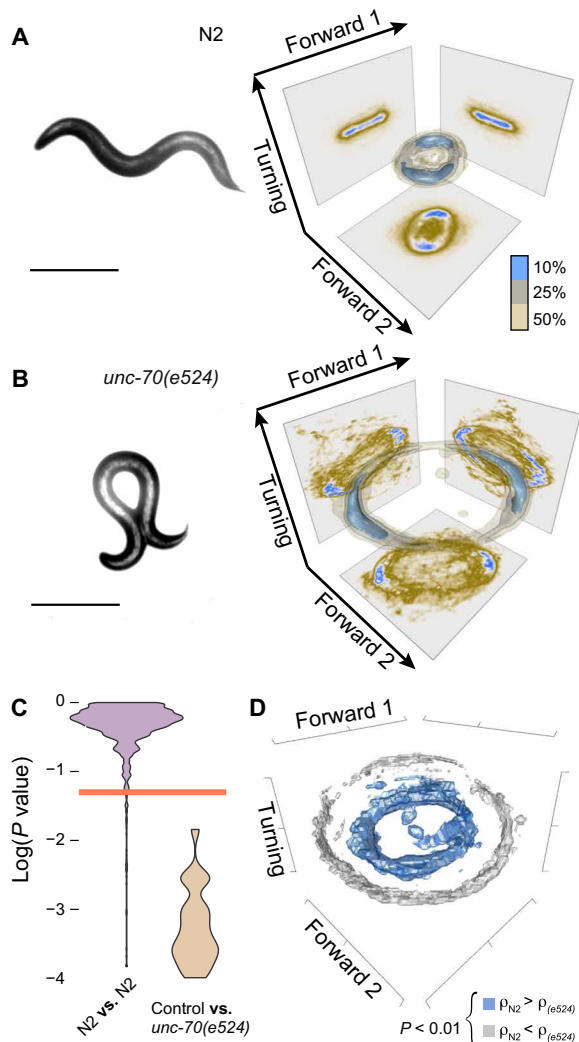
Fig. 1. β-Spectrin constrains the limit cycles during forward locomotion.
(**A** and **B**) Representative still image of (A) wt animals and (B) *unc-70(e524)* animals and the 3D density estimate for the joint probability distribution (equivalent to a discrete 3D histogram) of the two forward and turning modes in the eigenworm space. Color scale: brown, low density; blue, high density. Scale bars, 300 μm. (**C**) Violin plots of the *P* value distributions for 1000 independent tests of a bootstrapped population estimate of wt 3D probability density function (ctrl) tested against itself or a bootstrapped population estimate of *unc-70(e524)*. Orange line indicates α = 0.05 level of significance for the hypothesis H_0 that bootstrapped density functions derived from (A) and (B) are equal (see Materials and Methods). (**D**) Statistical test that the local kernel density function ρ of N2, as shown in (A), is larger (blue) or smaller (gray) than *unc-70(e524)*, as shown in (B). The test is performed on each voxel in a 100 by 100 by 100 grid (see Materials and Methods) and color-coded according to its outcome. Voxels with *P* >0.01 are not shown.

except for omega-turns, show little deviations into the third dimension during forward locomotion (Fig. 1A). The result is a planar, toroidal manifold as seen in Fig. 1A. In contrast, *unc-70(e524)* animals display much larger orbital trajectories, visible as an expansion of the toroid in the two forward modes, and substantial excursions into the turning mode (Fig. 1B), indicative for severely exaggerated body bends (Fig. 1, C and D). With this analysis, it becomes apparent that UNC-70 is required to reach and adjust the curvature amplitude during forward locomotion that is optimized for animal locomotion.

The spectrin network has cell-specific roles during locomotion

Because β-spectrin is expressed in many, if not all, neurons and weakly in body wall muscles (*20*, *24*, *25*), a higher bending amplitude could, in principle, reflect defects in muscle contraction or a loss of neuronal control. We therefore sought to test tissue-specific roles of β-spectrin independently and generated a "floxed" *unc-70* allele (Fig. 2A and see Materials and Methods for details) that allows for conditional excision upon cell-specific expression of the CRE recombinase in muscles or neurons and confirmed CRE activity using a fluorescent recombination reporter (fig. S1 and table S2) (*26*). Neither the CRE lines nor the floxed *unc-70* (fig. S2, A to D, K, and L) allele had a phenotype on its own when tested separately. Having successfully confirmed CRE activity, we pan-neurally expressed CRE in the floxed *unc-70* background (Fig. 2B and movie S2) and rarely observed a regular orbit in the eigenworm space of forward locomotion, as expected for severely uncoordinated locomotion behavior. When we expressed CRE under muscle-specific promoter (*27*), we did not observe any defect (Fig. 2C), suggesting that β-spectrin is functionally restricted to neurons during crawling behavior in adults.

We then expressed CRE in A-, B-, or D-type motor neurons or the previously proposed proprioceptors SMD, PVD, touch receptor neurons (TRNs), or DVA and confirmed successful recombination (fig. S1 and table S2). Although we neither detected a significant locomotion phenotype in A-, B-, and D-type motor neurons (fig. S2, E to G, and movie S2) nor in TRNs (fig. S2H) or PVD (fig. S2I), *unc-70* deletion in SMD caused subtle but significant defects (fig. S2, J and L), and only the knockout of *unc-70* in DVA (Fig. 2, D and F) consistently leads to an abnormally exaggerated body posture (movie 2) that can be rescued by a DVA-specific expression of full-length *unc-70* complementary DNA (cDNA) (Fig. 2E). To obtain DVA-specific CRE activity, we used a 300–base pair (bp) fragment of the *nlp-12* promoter that has been used in prior work to cell-selectively induce transgene expression in DVA (*23*, *28*) and showed recombination exclusively in DVA with our transgene (fig. S1I).

This observation motivated us to ask whether the restricted role of UNC-70 in DVA during movement was a general property of spectrin fibers or specific to β-spectrin. Thus, we knocked out SPC-1/α-spectrin, using the well established auxin-induced protein degradation (AID) system (*29*, *30*). We used a previously published SPC-1::AID animal (*31*) and first verified that the spatially restricted expression of TIR ligase in TRNs leads to a reduction in protein levels upon addition of auxin (fig. S3, A to D). Then, we targeted TIR to DVA and found that neither expression of the SPC-1::AID (fig. S3, E to H) nor the TIR ligase alone (fig. S3, I to L) but only the coexpression of both transgenes in DVA lead to exaggerated body angles, visible as a larger manifold in the eigenworm space (fig. S3, M to P), similar to the CRE-dependent *unc-70* knockout in DVA observed before (Fig. 2D). Together, our conditional gene ablation strategy unveiled an unexpected cell-specific role, of the otherwise widely expressed spectrin network, in regulating the extent of body bending during locomotion.

DVA activity correlated with compressive stresses in vivo
We next investigated whether changes in body postures influenced neuronal activity in DVA in an *unc-70*–dependent manner. We first generated a Ca^{2+} activity reporter using DVA-specific expression of
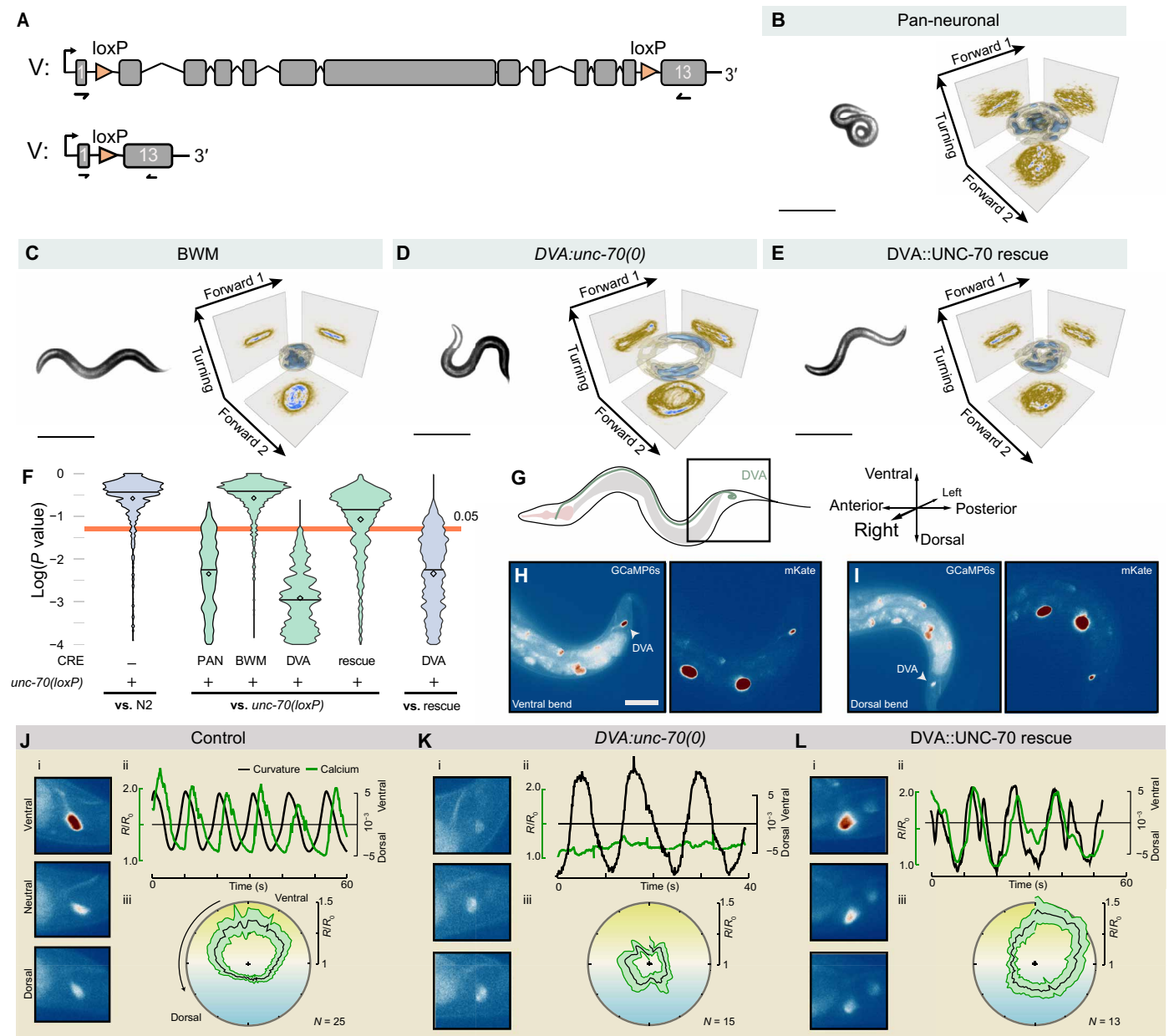
Fig. 2. β-Spectrin controls body posture specifically in DVA. (A) Genetic strategy for cell-specific deletion of *unc-70* in individual cells and neurons by flanking the *unc-70* genomic fragment with two loxP sites and the resulting genomic scar after recombination. (**B** to **E**) Representative still image and the corresponding manifold in the 3D eigenworm space for (B) PAN-neuronal *unc-70* deletion, (C) *unc-70(loxP)* animals with CRE-expression in body wall muscles (BWM), (D) DVA sensory interneurons, and (E) DVA-specific *unc-70* mutant expressing full-length *unc-70* cDNA under the *nlp-12* promoter. Scale bars, 300 μm. (**F**) *P* value distribution for 1000 independent tests for the hypothesis H_0 that the density functions for indicated combinations are equal (see Materials and Methods). Orange line indicates α = 0.05 level of significance. For *unc-70(loxP)* data, see fig. S2A. (**G**) Schematic of an animal with the location of DVA cell body and its axon and the coordinate system of our analysis. For clarity and convenience, we display ventral up to emphasize positive calcium correlation with ventral postures. (**H** and **I**) Representative calcium-sensitive (GCaMP6s) and calcium-insensitive (mKate) images for (H) ventral and (I) dorsal body bends. Scale bar, 50 μm. (**J** to **L**) Representative calcium imaging data from moving (J) control, (K) DVA-specific *unc-70* mutants [DVA::*unc-70(0)*], and (L) DVA::*unc-70(0)* with DVA-specific rescue expressing GCaMP6s calcium reporter in DVA subjected to ventral and dorsal bends. (i) Video stills of ventral, neutral, and dorsal bends. (ii) Time series of the normalized GCaMP/mKate ratio (left axis, green) and body curvature (right axis, black). (iii) Average GCaMP/mKate ratio plotted against the phase angle of body curvature. Yellow shading indicates ventral bends (top), and blue corresponds to dorsal body posture (bottom).

Gal4 driving a GCaMP6s effector (*32*). Then, we performed live imaging and video tracking to correlate Ca²⁺ activity and body curvature in proximity to the cell body (square in Fig. 2G) and normalized the Ca²⁺-sensitive by a Ca²⁺-insensitive fluorophor (Fig. 2, H and I). Although the low Ca²⁺ signal exhibited occasional spontaneous

activity bursts and low-amplitude spontaneous signals in completely restrained animals (fig. S4A), we observed notable activity changes between the ventral and the dorsal side in animals undergoing body swings with amplitudes characteristic for forward locomotion (Fig. 2J and movie S3). We expected activation in the cell body to

occur when the portion of DVA's axon closest to the cell body is stretched when the worm is locally bending dorsally. Instead, activation was correlated with ventral bends, which cause local shortening of the axon (fig. S5A).

To understand the role of UNC-70 in this process, we repeated these experiments in the *unc-70(e524)* mutation (fig. S4B) and in the DVA-specific *unc-70* knockout (Fig. 2K and movie S3B). Under both conditions, we did not observe curvature-correlated Ca^{2+} activity, suggesting that β-spectrin is needed for neuronal activation as a response to body posture changes. Rarely, however, signals also appeared during dorsal bends, indicating that UNC-70 directs the preference of neuronal activation during ventral postures in wt animals (fig. S9D). The effect of the conditional unc-70 loss of function can be rescued by a DVA-specific expression of *unc-70* (Fig. 2L and movie S3C), further indicating that the spectrin cytoskeleton acts cell-autonomously within DVA.

We next investigated whether tensile stresses from the anterior dorsal curvature influence the Ca^{2+} signals measured in the posterior cell body when the tail bends ventrally. We thus repeated our calcium imaging experiment in a microfluidic chip with a trapping channel of defined curvatures that are characteristic for forward crawling [a device termed waveform sampler (WFS); see below and (*33*)]. Therein, individual animals can be hosted with a single, defined curvature at a given time. To do so, we first "parked" an animal in a straight position of the WFS before a bend and then gently pushed it into either a dorsal bend or a ventral bend (Fig. 3A) under which DVA becomes passively stretched or compressed, respectively, while recording dual color fluorescence videos (Fig. 3B and movie S4). Similar to our observation in freely crawling animals (Fig. 2J), we consistently observed DVA calcium activity increases during these passive, ventral bends (Fig. 3, D and E). In contrast, we observed that, during dorsal bends, Ca^{2+} activity decreased but quickly returned to fluorescence levels once the animal was straight again (Fig. 3, D and E). This analysis indicates that a single curvature close to the tail elicits robust Ca^{2+} transients under compression or under tension relaxation. In summary, because we did not observe any Ca^{2+} increase in the DVA cell body when anterior body parts were bent we concluded that Ca^{2+} signaling originated upon ventral bends and remained confined locally.

β-Spectrin is under compression during ventral body bends

The finding that DVA activates during ventral bends primed us to investigate how mechanical stresses affect axon shape in moving animals and how the spectrin network contributes to proprioceptive mechanosensitivity. We thus recorded short videos and quantified the local length changes of DVA in each frame as a function of body posture in flexing animals (fig. S5). Similar to ventral TRNs [e.g., AVM (*20*, *34*)], DVA locally shortens and elongates up to 40% (fig. S5A and movie S5) during dorso-ventral swings in wt animals. In *unc-70(e524)* and DVA-specific β-spectrin mutants, however, DVA extended under dorsal body postures but failed to shorten during ventral bends (fig. S5, B and C). Instead, the axon showed a shape change characteristic of a mechanical failure due to compressive stresses, known as buckling instability (movie S5).

Physical intuition teaches us that an elastic body subjected to bending experiences compression on the concave and extensions on the convex side (*35*, *36*), with a stress σ that increases with the distance to the central axis (*d*), elasticity of the worm's body (*E*), and the curvature assumed (*c*; Fig. 4A). These principles are formulated in the Euler-Bernoulli beam bending equations as σ = *dcE* (*35*, *36*). Because the thickness of the animals does not change during locomotion and at the slow dynamics inherent to biological systems, *E* is likely constant over all body posture, we postulate that changes in body curvatures lead to changes in stress. To directly visualize the stresses originating in the body of *C. elegans* in postures that are typical during locomotion, we resorted to a previously characterized fluorescence resonance energy transfer (FRET) tension sensor (*20*, *37*), with predominantly neuronal expression (fig. S6, A and B). The inherent mobility of *C. elegans* precluded unrestrained imaging; thus, we redesigned a microfluidic device (*33*) with channels of varying curvatures (Fig. 4, B and C) that could trap animals in different postures for 3D imaging (Fig. 4D). In completely straight positions, FRET values were evenly distributed on the ventral and dorsal side of the animals (Fig. 4E). When the same animal was bent inside the channel, the concave side had a higher FRET efficiency than the convex side in a curvature-dependent manner (Fig. 4, E and F), indicative for a differential compression and extension of the animal's body. However, these differences in FRET between the convex and concave side were not observed in a stretch-insensitive sensor that was fused to the N terminus of the protein, such that it could not be pulled apart and report tension (Fig. 4, G and H), or in a constitutive high-FRET and low-FRET construct in which the elastic force sensor domain was replaced with a stiff 5– or 200–amino acid linker domain (fig. S6, E to H). We next sought to investigate whether this distribution of bending
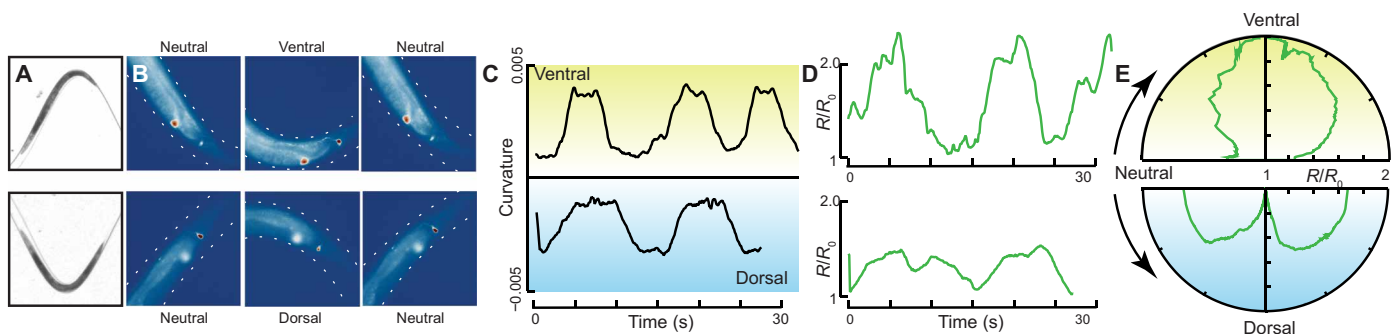

Fig. 3. DVA responds differently to curvature-induced stretch and compression in vivo. (**A**) Position of the animal in the microfluidic channel for curvature-induced calcium recordings. (**B**) Representative snapshot of an animal before, during, and after being subjected to a single ventral (top) and dorsal (bottom) curvature close to the tail. (**C** and **D**) Quantification of (C) curvature and (D) normalized GCaMP/mKate ratio during the mechanical manipulation. (**E**) GCaMP/mKate ratio plotted against the phase angle of body curvature, representative for six animals. Yellow shading indicates ventral bends (top), and blue corresponds to dorsal body posture (bottom).
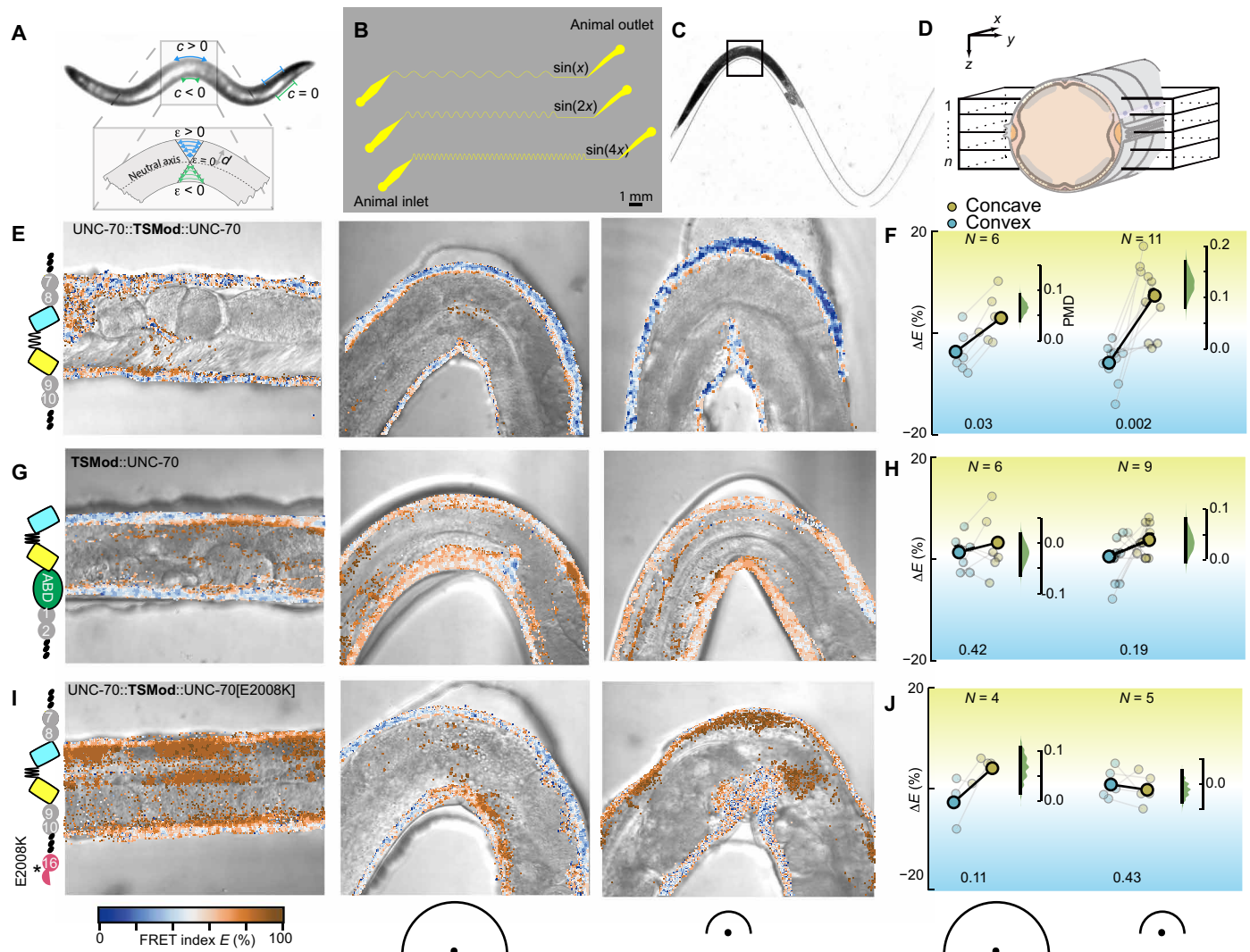
Fig. 4. Changes in body mechanics encode body posture curvature. (**A**) Schematic of a crawling animal with varying posture along its body and the associated Euler strains. c, curvature; ϵ, strain; d, thickness. (**B**) Sketch of the mask layout with varying channel curvatures and periodicities. (**C**) Bright-field (BF) image of an animal inside the $\sin(2x)$ channel. (**D**) 3D representation of the image acquisition procedure. A volume consisting of 10 to 15 frames encompassing the ventral and dorsal nerve chord was acquired, omitting the lateral nerves. (**E, G**, and **I**) Schematic, representative, and FRET images of collapsed z stacks for straight and increasingly curved channel of the WFS chip with the FRET index map overlaid on top of a BF image for (E) UNC-70::TSMod force sensor with full-length UNC-70 β-spectrin bearing TSMod embedded between spectrin repeats 8 and 9, (G) force-insensitive FRET control with the TSMod fused to the N terminus of full-length β-spectrin, and (I) UNC-70::TSMod(E2008K) mutant force sensor. Dark pixels indicate autofluorescence from the gut. Color scale indicates FRET indices, half circles indicate curvatures of the trapping channel, and larger circle indicates smaller curvature. (**F, H**, and **J**) Quantification of the FRET index difference between the convex and concave side of the body and a straight position of the same animal. $\Delta E > 0$ indicates compression, and $\Delta E > 0$ indicates tension. Each connected pair is derived from one image; bold connected dots indicate mean of the sample. The floating right axis shows the paired mean difference (PMD) as a bootstrap sampling distribution (green) and the 95% confidence interval as a vertical black line. Numbers below the graph indicate the P values for the likelihood of observing the effect size, if the null hypothesis of zero difference is true.

stresses is changed in animals mutant for β-spectrin that leads to exaggerated body bends and the loopy phenotype (Fig. 1B). We thus engineered a β-spectrin tension sensor bearing the E2008K mutation (see Materials and Methods) and found that these animals had consistently higher FRET values in neurons than control animals (fig. S6, C and D), indicative for a lower neuronal tension. Likewise, after performing FRET imaging of the E2008K spectrin mutant animals in the curved channels of our microfluidic device, we failed to detect differences in FRET efficiencies between the compressed (concave) and stretched (convex) side at high curvatures

(Fig. 4, I and J), indicative for a failure of the mutant β-spectrin to sustain compressive and tensile mechanical stresses. We conclude that the E2008K mutation does not interfere with formation of the ubiquitous α/β-spectrin network [see fig. S6, I and J, and (34)], as judged by the α-spectrin periodicity in the β-spectrin *unc-70(e524)* point mutation. Together, this shows that the spectrin cytoskeleton sustains compressive and tensile stresses during body bending. We further conclude that changes in body curvature are encoded in the mechanical state of the spectrin network, which conveys mechanical stresses to activate DVA.

UNC-70 requires TRP-4 mechanosensitive ion channel to limit body bends

Our notion that DVA-specific mutations of *unc-70* increase body curvature (Fig. 2D) is shared by the function of the mechanosensitive NOMPC homolog TRP-4 in DVA (*4*), suggesting a functional relation between UNC-70 and TRP-4. Animals bearing the *trp-4(sy695)*, and occasionally in *trp-4(ok1605)* single mutation (table S1), have significantly different locomotion phenotypes as compared to wt animals (Fig. 5, A and D, and movie S6). Because we were able to rescue this locomotion defect by expressing full-length *trp-4* cDNA

with the DVA-specific *nlp-12* promoter, this exaggerated body bending phenotype in the *trp-4* mutation is likely due to defects in DVA (Fig. 5B and movie S6). The observation that *unc-70* and *trp-4* share functions in regulating body posture during locomotion primed us to ask whether UNC-70 and TRP-4 act within the same or within a separate parallel mechanical pathway. To determine whether UNC-70 and TRP-4 function together in determining the body posture during locomotion, we generated animals carrying *trp-4(sy695)* and *unc-70(e524)* double mutations and *trp-4(sy695)* together with a DVA-specific defect of *unc-70*. Under the notion
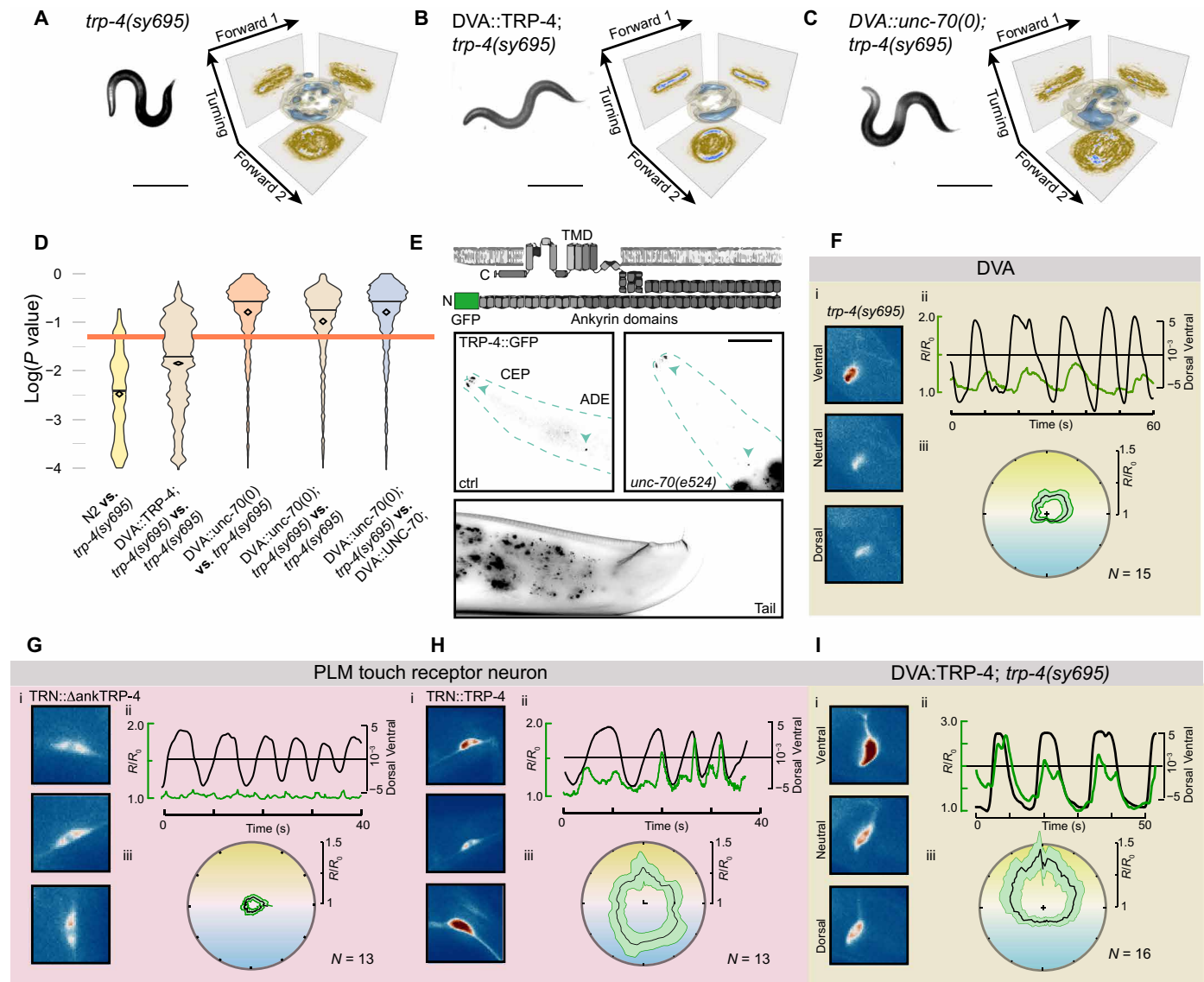

Fig. 5. TRP-4 activity is required but not sufficient for locomotion and DVA mechanosensitivity under compression. (**A** to **C**) Representative still image and the corresponding manifold in the 3D eigenworm analysis for (A) *trp-4(sy695)* mutant animals, (B) *trp-4(sy695)* mutant animals carrying DVA-specific *trp-4* rescue, and (C) *trp-4(sy695);DVA::unc-70* double mutants. (**D**) P value distribution for 1000 independent tests for the hypothesis H₀ that the density function for indicated combinations are equal (see Materials and Methods). Orange line indicates α = 0.05 level of significance. (**E**) Schematics of the TRP-4::GFP CRISPR knock-in and representative images of the head and the tail in wt and *unc-70(e524)* background. Scale bars, 30 μm. (**F** to **I**) Calcium imaging data from moving animals, (F) DVA neuron in *trp-4(sy695)* mutant, (G) PLM in an animal expressing N-terminally truncated TRP-4, (H) PLM in animals expressing full-length TRP-4, and (I) DVA neuron in *trp-4(sy695)* mutant expressing *trp-4* cDNA under the *nlp-12* promoter to rescue in DVA. (i) Video stills of ventral, neutral, and dorsal bends. (ii) Time series of the normalized GCaMP/mKate ratio (left axis, green) and body curvature (right axis, black). (iii) Average GCaMP/mKate ratio ± SE plotted against the phase angle of body curvature.

that spectrin and TRP channel are causally dependent and act in series within the same pathway, we expect no additive effect of the double mutation. If these gene products, however, act in two redundant, parallel pathways, then the mutation of both genes will likely result in a more severe phenotype of the double mutation than either single mutant alone. When we assayed locomotion of the double mutations with *trp-4* and two different *unc-70* alleles, we generally did not observe a more exaggerated body posture than in either single mutation alone (Fig. 5, A, C, and D). We also confirmed that the *unc-70(e524)* mutation does not interfere with TRP-4 localization and generated endogenously tagged green fluorescent protein (GFP)::TRP-4 by CRISPR (*38*). Expression levels of TRP-4 in DVA remained below background autofluorescence (Fig. 5E), and we restricted our analysis to the cilia of CEP or sensilla of ADE, which locally enrich the protein in sensory endings. The distribution and trafficking of endogenously tagged TRP-4 into the distal part of the sensory endings is unaffected by the E2008K spectrin mutation. Together, our data suggest that *unc-70* and *trp-4* do not have redundant, compensatory roles to limit body bending amplitude during locomotion.

TRP-4 is dispensable to elicit curvature-dependent calcium activity in DVA

We next analyzed whether compression-induced Ca^{2+} signals depend on the TRP-4/NOMPC ion channel. Spontaneous activity in immobile *trp-4* mutant animals was strongly reduced, with occasional decreases in Ca^{2+} signals (fig. S4C). However, when we performed Ca^{2+} imaging in flexing animals, we still observed DVA Ca^{2+} activity during ventral body bends in *trp-4(sy695)* mutant animals, although these DVA signals were less modulated by swings in body curvature (Fig. 5F). This analysis shows that TRP-4 expression is dispensable for compression-induced Ca^{2+} signal during body bending. We were thus wondering whether TRP-4 is sufficient to sensitize otherwise motion-insensitive neurons lacking endogenous TRP-4 expression (*39*), to activate during dorso-ventral body bends. We hence expressed full-length *trp-4* cDNA and an N-terminally truncated construct in TRNs, the gentle body touch mechanoreceptors (*35*). In wt animals (fig. S4D) and transgenics expressing the truncated isoform (Fig. 5G), basal Ca^{2+} levels measured in PLM rarely changed and are seemingly uncorrelated with body curvature in slowly moving animals. However, upon expression of full-length TRP-4 in TRNs, we observed a strong periodic signal in PLM during body bending that correlated well with body bends (Fig. 5H). We also frequently observed increases in PLM activity when the animal bent toward both the dorsal and ventral sides (Fig. 5H). To further confirm that TRP-4 acts in DVA to modulate calcium transients during body flexing in our experimental paradigm, we directed the expression of full-length *trp-4* cDNA under the *nlp-12* promoter. Consistent with a DVA-specific role of TRP-4 in locomotion, we were able to rescue the subtle decrease in Ca^{2+} signaling (Fig. 5I). Together, TRP-4 can, in principle, endow curvature sensitivity in heterologous neurons but is dispensable for curvature-induced DVA activity.

DVA responds differently to tension and relaxation gradients in vitro

We then established a primary culture of *C. elegans* neurons (*20*) on compliant polydimethylsiloxane (PDMS) surfaces and verified that DVA expressing GCaMP6s robustly activated in response to substrate deformation (Fig. 6A). Cultured DVA neurons repetitively elicited high Ca^{2+} transients (Fig. 6, B and C, and movie S7) that partially depended on functional TRP-4 expression and could be blocked by nonspecific cation channel inhibitor $GdCl_3$ (Fig. 6D). Most notably, we frequently found that DVA neuron became active during the force offset (Fig. 6, B and C) and buckled during indentation, suggesting that they sensed negative tension gradients or compression.

Because PDMS substrate deformation induces compressive and tensile stresses along the axon at the same time, we specifically applied positive and negative tension gradients to isolated axons (Fig. 6, E and F) and visualized their resultant Ca^{2+} transients using confocal microscopy (fig. S7A). To do so, we used optically trapped microspheres and extruded single membrane tethers (*40*) from DVA axons (Fig. 6E) with varying velocity. The resulting tether force increased with the pulling velocity but quickly relaxed to a static value (Fig. 6G) when the movement ceased. Using this approach, we measured local gradients that were 100× higher than the resting membrane tension (≈ 2 mN/m; fig. S7B), resulting in a rich behavior in the Ca^{2+} dynamics. Notably, Ca^{2+} signals increased preferentially during the relaxation phase of the force-distance cycle directly at the tether neck (Fig. 6, F to H, and movie S8), indicating that negative tension gradients, similar to axon compression in vivo (fig. S5A), can induce neuronal activity (Fig. 2J). In *trp-4* mutants, however, we did not observe an increase in Ca^{2+} activity during tension relaxation (Fig. 6, I and J). The Ca^{2+} preference for relaxation could be partially recovered in rescued mutant DVA that express *trp-4* cDNA under the *nlp-12* promoter (Fig. 6, I and J). In addition to the Ca^{2+} increases during tether relaxation in wt neurons, we also frequently observed a transient reduction in Ca^{2+} signals during tether extrusion, especially at higher velocities (Fig. 6, F to H), suggesting that the concomitant increase in membrane tension (Fig. 6, E to G) suppresses neuronal activity.

How does an increase in membrane tension lead to decrease in calcium signal? This observation, in principle, can be explained, in part, because of the existence of a stretch-activated potassium channel that deactivates the neuron under tension. To understand the observed Ca^{2+} dynamics, we set up a computational model (*41*), in which positive and negative forces selectively activate hyperpolarizing and depolarizing ion channels, respectively. We illustrate this scenario with two hypothetical, mechanosensitive ion channels acting as primarily sodium/calcium conductive (depolarizing) and a potassium conductive (hyperpolarizing) and model channel gating under force as a thermally driven escape over a potential barrier (*42*) (fig. S7E; for details see the Supplementary Materials). Consistent with previous results derived from electrophysiological recording of TRP-4–expressing CEP (*43*), we modeled sodium activity at the force onset and offset by sensitizing it to the loading rate (Fig. 6K, i and ii), while K^+ channel displayed activity only during force onset (Fig. 6K, iii). With realistic ion channel parameters taken from the literature (see the Supplementary Materials) and assuming a constant input resistance, the open probability of the K^+ channel was able to completely suppress the Ca^{2+} channel–induced neuron activity at the force onset but not when the force was released (Fig. 6K, iv). Although our calculation does not include the complex regulation and spontaneous Ca^{2+} dynamics that likely take place inside a cell, our reductionist model is in good match to the experimentally determined DVA activity (Fig. 6G), such as a transient Ca^{2+} decrease during extension and transient rise due to relaxation. We next sought to test this prediction.
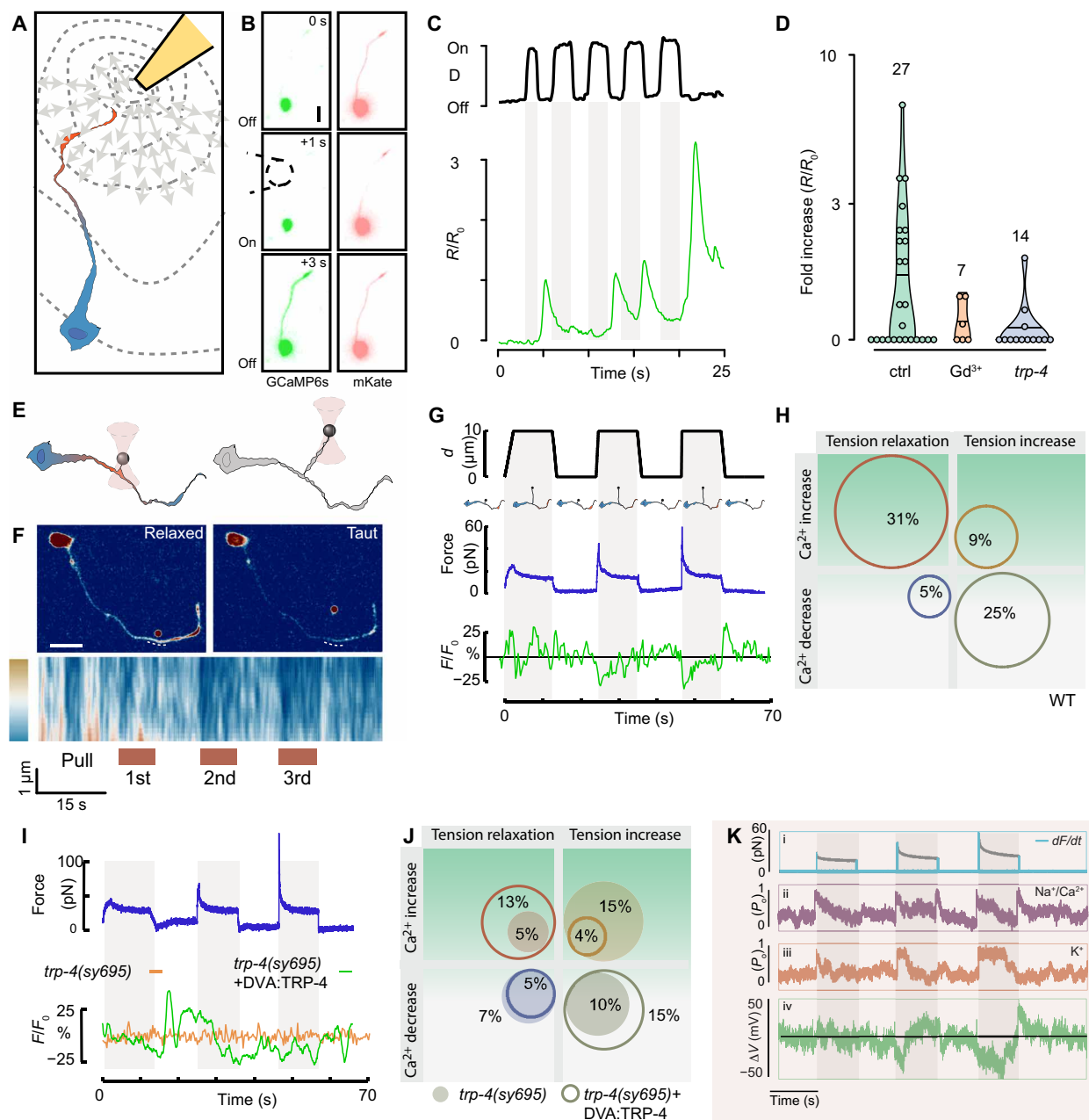
Fig. 6. Opposing membrane tension gradients modulate DVA activity in vitro through TRP-4 and TWK-16. (**A**) Schematic of the PDMS stretching experiments. (**B**) Three successive images of the Ca^{2+}-sensitive (left) and Ca^{2+}-insensitive (right) dye of an isolated DVA subjected to substrate deformations. (**C**) PDMS substrate deformation D (black line) and GCaMP/mKate ratio (R/R_0, green line) plotted against time. (**D**) Violin plot of the Ca^{2+} activity derived from control (ctrl), ctrl treated with Gd^{3+}, and *trp-4(sy695)* mutant DVA neurons. (**E**) Schematics of the dynamic tether extrusion experiments. (**F**) Representative still images of the GCaMP signal from an isolated DVA neuron before and during tether extrusion. Dotted line indicates the location of the kymograph displayed below showing the temporal evolution of the Ca^{2+} signal at the tether neck. (**G**) Representative displacement (d), force, and normalized Ca^{2+} signal extracted from the experiment in (F). (**H**) Bubble plot of the relative number of events (probability) that a tether extrusion or relaxation leads to an increase or decrease in GCaMP activity in wt DVA neurons. $N = 48$ cells. (**I**) Representative force trace and normalized Ca^{2+} transients for *trp-4* (orange) mutant cells and mutant cells expressing a *trp-4* rescue transgene (green trace). (**J**) Bubble plot of the probability that a tether extrusion or relaxation leads to an increase or decrease in GCaMP activity in DVA neurons mutant for *trp-4*, $N = 38$, mutant cells (filled circles). Distribution of Ca^{2+} activity in DVA rescue cells are shown as open circles. (**K**) In silico study of the optical trapping experiment. (i) Simulated force (black trace) and temporal tension gradients (light blue). (ii and iii) Open probability of the hypothetical Na^+ and K^+ channel. (iv) Sum of a current through a linear combination of its average open probability × single channel conductance. Note that the double peak in the purple trace becomes suppressed because of simultaneous activation of the inhibitory signal, giving rise to the experimentally observed behavior.

The K2P homolog TWK-16 suppresses Ca²⁺ activity during dorsal posture

The results of our simple kinetic model predicts that the Ca^{2+} signals at the force onset becomes unmasked in absence of inhibitory, potassium activity. DVA is one of the few neurons that expresses the mechanically regulated leak potassium channel TWK-16 (44, 45), a TREK2 homolog of mechanosensitive, two-pore K^+ channels (46) in *C. elegans*. We thus repeated the dynamic tether extrusion experiment in a *twk-16* null mutant background (Fig. 7, A and B) and measured the concomitant change in GCaMP intensity. Consistent with our hypothesis, we did not observe a Ca^{2+} decrease during tether pullout, indicating that mechanical deactivation at high membrane tension gradients is *twk-16* dependent. Instead, we frequently observed a Ca^{2+} increase at the onset of the tether extrusion (Fig. 7, A and B), as if TWK-16 functions in suppressing tension-induced activity normally observed in TRP-4–expressing neurons (43). The notion of stretch-induced suppression of Ca^{2+} activity through TWK-16 in isolated DVA neurons raises the question of whether TWK-16 is a functional component during proprioception. To answer this, we first repeated the Ca^{2+} imaging of DVA in moving *twk-16* mutant animals. Compared to wt animals, we found that the deletion of *twk-16* caused a subtle increase in Ca^{2+} activity in DVA during spontaneous body bending (Fig. 7C), especially at dorsal postures, with an overall unchanged ventral preference. Nevertheless, we frequently observed GCaMP intensity changes during dorsal posture and even during both, dorsal and ventral posture (Fig. 7C and fig. S9H), a signature that we never observed in DVA of wt animals but occasionally in *unc-70* mutants (Fig. 2L) and ectopic expression of TRP-4 in TRNs (Fig. 5H). Together, this suggests that TWK-16 is able to suppress Ca^{2+} transient at dorsal posture, when DVA experiences mechanical tension, similar to how tension suppresses calcium activity in our in vitro experiment (Fig. 6).

We then asked whether TWK-16 expression in DVA is required for animal locomotion. In contrast to *trp-4* animals, we observed a subtle but significant difference between the wt and *twk-16* null mutant of their 3D densities in the eigenworm space, as an indicator for a reduced body bending amplitude (Fig. 7D and fig. S8, A to C). TWK-16 is also expressed in other neurons, including AVK that counteracts DVA activity (23). First, we inserted an AID:wScarlet tag (29) at the TWK-16 C terminus, verified expression in DVA (fig. S8D), and confirmed that the fusion protein did not cause any locomotion defects in absence and presence of auxin (fig. S8, E to G). Then, we expressed the previously characterized TIR ligase (fig. S3, I to L) together with the TWK-16::AID and repeated the behavior experiment. Although we already noticed an auxin-independent effect (47) on body bending amplitude (Fig. 7E), the addition of 1 mM auxin caused a marked reduction of body bending amplitude compared to wt and a clearly distinguishable eigenworm representation (Fig. 7, D and E; fig. S8, H to J; and movie S9). Together, TWK-16 inactivates DVA under tension and counteracts TRP-4 depolarization with DVA-specific function in locomotion.

Compression-induced activity adjusts motor output in a neuronal network model

The known wiring diagram of *C. elegans* offers the opportunity to ask how the observed neuronal activity changes are processed on the nervous system level. To interrogate how the compressive proprioception of DVA adjusts the motor circuit (Fig. 8A) and affects *C. elegans* locomotion, we adapted a well-established neuro-mechanical model (48) that was previously deployed to simulate the effect of stretch-sensitive feedback embedded directly into the motor neurons. In our modification, we consider a single compression-sensitive current during ventral bends, matching our notion that DVA is excited during ventral curvatures. In agreement with the connectivity of the *C. elegans* network, DVA directly informs the motor neurons on the dorsal side (49, 50). In this scenario, the simulation of compressive sensitivity during ventral bends but not stretch sensitivity during dorsal bends produced a crawling pattern seemingly similar to experimental results (Fig. 8B). With the aim to understand how the compression-current sensitivity influences crawling pattern, we reduced the responsiveness to compression, compatible to the *unc-70* and *trp-4* mutations in the experiments (Figs. 2 and 5). Notably, the simulation recapitulated the crawling behavior observed under the mutant conditions, visible as an expansion of the manifold in the eigenworm state space (Fig. 8C and movie S10).

DISCUSSION

Proprioceptive and visceral mechanosensation are vitally important processes ensuring body homeostasis and organ function. Here, we genetically, mechanically, and computationally deciphered the molecular underpinnings that determine the shape of the limit cycle attractor during *C. elegans* locomotion. We used a well-characterized mechanical stress sensor (20, 51) in combination with neuronal activity indicators and revealed that DVA activates under compressive stresses in an UNC-70 β-spectrin–dependent manner. This apparent discrepancy in light of the classical view of mechanical stretch reception is not a sole feature of DVA but has previously been observed in other *C. elegans* proprioceptors such as SMD (6), *Drosophila melanogaster* multidendritic class I proprioceptors (52), which preferentially activate in a direction-selective manner when the contracting segment gets compressed (52), and mechanosensory neurons regulating thirst in the mammalian brain (53). Latter is directly sensed by volume changes through a specific TRPV1-microtubule interaction when neurons lose water, and the membrane-bound ion channels push against the highly interweaved microtubule cytoskeleton, thus activating the neurons (53). It seems plausible that this "push-activation" model also accounts for the activation of the pentascolopedial chordotonal organs in the fruitfly, which have been shown to activate under compressive stresses during locomotion (54) in a NOMPC-dependent manner. The TRP family member NOMPC also interacts with a specialized microtubule cytoskeleton (55, 56), which conveys mechanical stress to the gating pore through a conserved ankyrin spring. Whether tension (57) or compression (16, 17) of the ankyrin repeats leads to mechanical gating of the pore remains to be determined; nonetheless, the application of membrane tension was not sufficient to activate mammalian TRP channel homologs (58). Likewise, our results from the truncated TRP-4 lacking ankyrin domain (Fig. 5G) suggest membrane-independent activation mechanisms. TRP and TransMembrane channel (TMC) channels are not the only ones implicated in compression sensing. Recent work demonstrated that a normal force of 50 pN is sufficient to cause conformational change in PIEZO1 (59), providing a plausible mechanism for compressive mechanosensitivity (60, 61). Our work showing compressive mechanosensitivity in vitro and in vivo thus motivates us to rethink the operation of "stretch"-sensitive
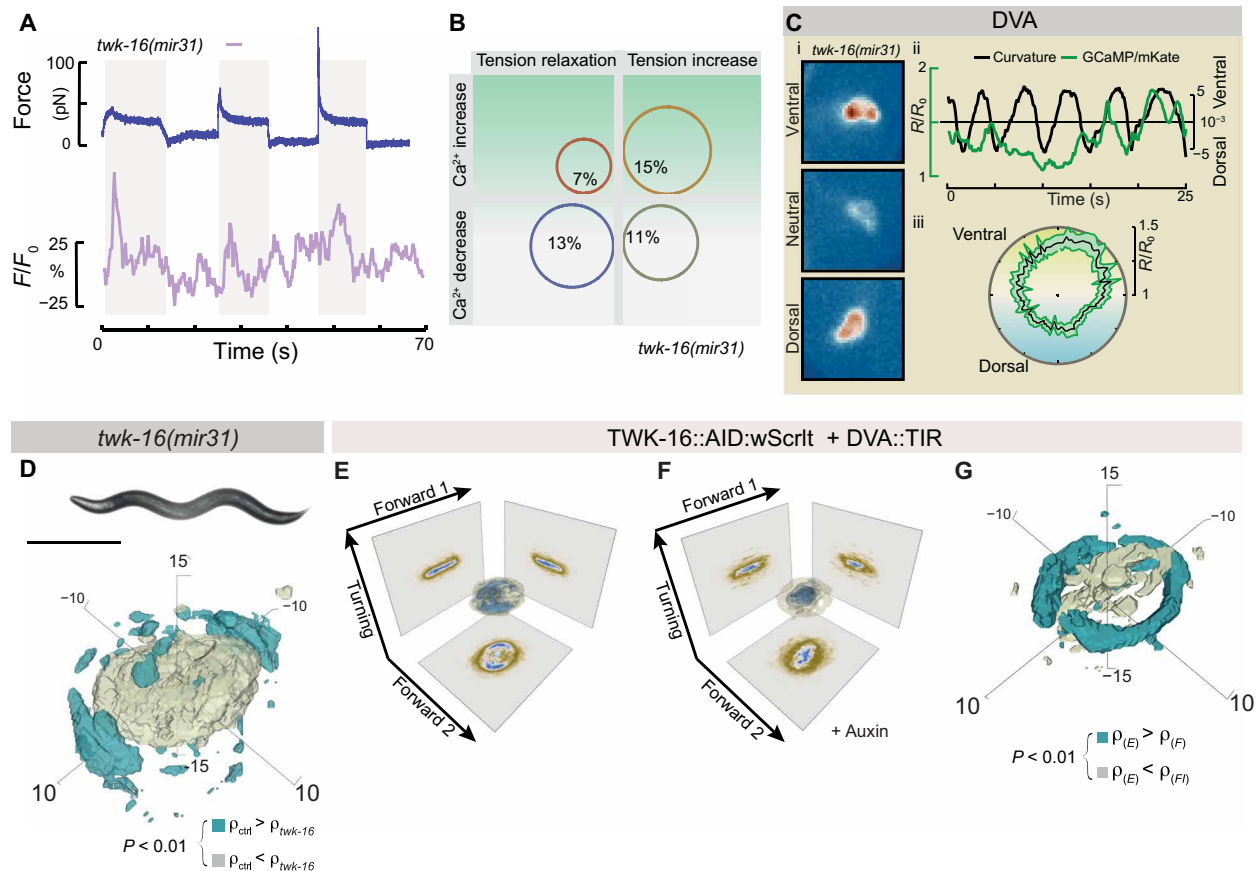
Fig. 7. TWK-16 suppresses bending excursions through modulation of DVA activity. (A) Representative force trace and normalized Ca^{2+} transients for *twk-16* (purple) mutant cells. **(B)** Probability that a tether extrusion or relaxation leads to an increase or decrease in GCaMP activity in DVA neurons mutant for *twk-16*, $N = 31$, mutant cells. **(C)** DVA Ca^{2+} data of *twk-16(mir31)* animal lacking functional TWK-16. (i) Video stills of DVA cell body during ventral, neutral, and dorsal bends. (ii) Time series of the normalized GCaMP/mKate ratio (left axis, green) and body curvature (right axis, black). (iii) Average GCaMP/mKate ratio ± SE plotted against the phase angle of body curvature. **(D)** Representative image of a *twk-16(mir31)* animal and the color-coded, statistically significant differences in the local probability density functions between control and *twk-16*. Scale bar, 300 μm. **(E and F)** 3D kernel density function (histogram) in the 3D eigenworm space for TWK-16::AID::wScarlet animals expressing TIR in DVA in (E) absence and (F) presence of auxin. **(G)** Color-coded, statistically significant differences in the local probability density functions between (E) and (F). Blue voxels indicate higher local density for untreated, and beige voxels indicate higher density for auxin-treated animals on the α = 0.01 level.

mechanoreceptors. Thus, our work complements computational results (*17*), suggesting that TRP-4/NOMPC ion channels are gated by compression of their ankyrin spring.

Previous work with first-generation G-CaMP calcium indicators established that TRP-4 is essential for curvature-induced DVA activity (*4*). Our in vivo Ca^{2+} imaging of DVA with GCaMP6s in the *trp-4(sy695)* mutation (Fig. 5F) reveals a shallower modulation and overall smaller amplitudes than wt neurons but does not eliminate curvature-induced Ca^{2+} signal. The notion that these signals do not depend on *unc-13* (*4*) and the residual mechanosensitive activity of isolated DVA on PDMS substrates (Fig. 6D) suggests that the remaining signal is generated DVA-autonomously by a yet unknown, redundant MeT channel. TRP-4 is not the only mechanosensitive ion channel expressed in DVA but might share function with DEL-1, TRP-1, TRP-2, and possibly others (*62*). Future work thus needs to address whether multiple ion channels contribute to the overall mechanosensing in DVA.

To profile the functional importance of the postembryonic spectrin cytoskeleton during *C. elegans* locomotion, we used cell-specific conditional strategies (CRE/lox; AID) and created mutations

that are restricted to single neuronal classes and tested the specificity of this approach using a fluorescent recombination reporter (fig. S1) (*26*). Despite the ubiquitous expression of UNC-70 β-spectrin and SPC-1 α-spectrin in most, if not all, neurons, we only observed a consistent phenotype after driving CRE enzyme using the *nlp-12p* promotor. Although *nlp-12* is reportedly expressed in other cells, including PVD neurons (*5*), our minimal 300-bp promoter transgene expression is mostly restricted to a single cell in the tail (table S2), suggesting that β-spectrin has specific roles restricted to DVA.

What interferes with DVA mechanosensing in the spectrin mutation? Our genetic analysis suggests that the spectrin network and TRP-4 act in the same process, e.g., during force transmission. We performed a coimmunoprecipitation of TRP-4 and UNC-70 as well as SPC-1 from Chinese hamster ovary cells but could not detect a direct biochemical interaction in this assay. Hence, we propose that indirect force transmission takes place involving stress propagation through local and global axon mechanics. We showed that DVA axons in *unc-70* mutations undergo buckling instabilities (fig. S5 and movie S5), which could, similar to events in TRNs, cause a marked reduction in the number and length of microtubules
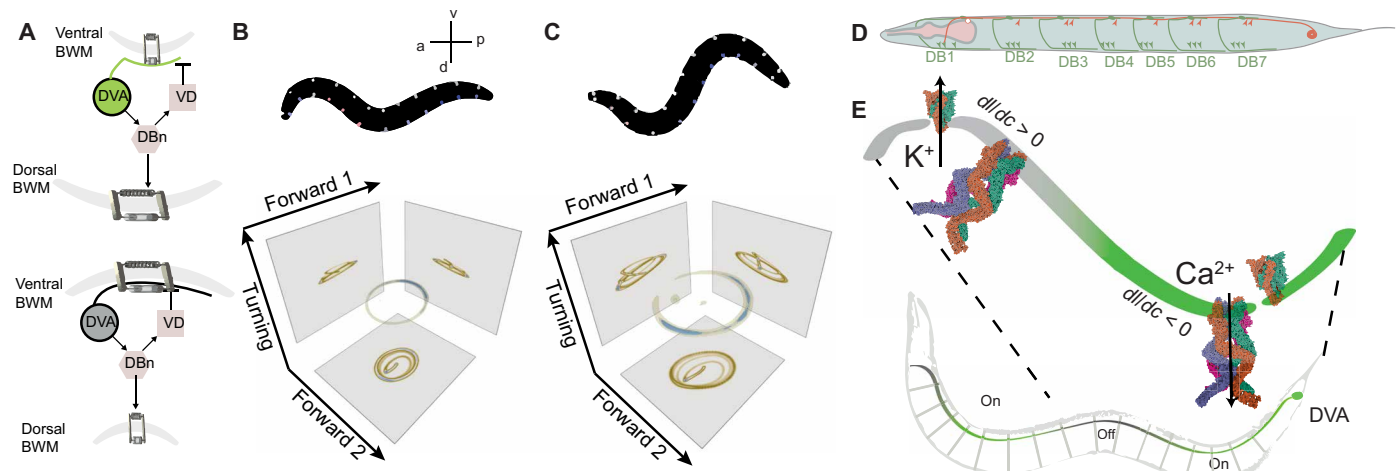
Fig. 8. Compression in DVA provides proprioceptive feedback to the motor circuit. (**A**) Schematic of the model formulation. A passive mechanical body is modeled as a lightly damped elastic beam (passive Kelvin-Voigt material) (*48*) in parallel with the muscles, as an "active" Kelvin-Voigt material with stiffness governed by the state variable of the motor circuit (through neuronal input). DVA senses compression during ventral bends and informs the DB neurons, which, in turn, activate dorsal muscle contraction and at the same time connect to inhibitory VD motor neurons, resulting in the relaxation of the ventral muscles. Under dorsal bends, DVA activity is suppressed (bottom). (**B** and **C**) A representative snapshot from the simulation of (B) wt and (C) "mutant" with reduced sensitivity to compressive stresses and the corresponding manifold in the eigenworm state space. Dorso-ventral circles depict motor neurons and their stretch receptor input. Blue, off; red, on. Ventral motor neurons are white, as they do not receive stretch receptor input. (**D**) Schematic of an animal indicating the synapses between DVA and dorsal B-type motor neurons based on (*49, 50*). Orange arrows, DVA→MN; green arrow, MN→BWM; circle, gap junction. (**E**) Illustration of the mechanical scenario under which neuronal tension hyperpolarizes (activates TWK-16/TREK potassium channels, orange) and compression depolarizes (TRP-4/NOMPC, blue) neuronal segments. Hyperpolarized domains thus limit the extension and spread of the signal along the length, thus leading to effective compartmentalization.

(*34*), consistent with curvature-induced fracture during buckling (*63*). This disintegration and disassembly of the load bearing microtubule filaments during cyclic strains conform to fluidization of the cytoskeleton (*64*), which constitutes a plausible mechanism of how a single point mutation in spectrin could interfere with efficient force transmission to the ion channel: the loss of tension sets the origin of the fluidization with vanishing stiffness (*65*) and thus a failure to build up, transmit, and convert compressive stresses from the cytoskeleton into ion channel opening.

For long axons, the question immediately arises: How a curvature sensitive neuron is able to process negative and positive curvatures and coordinate downstream motor neuron activity? DVA has a single neurite that spans the entire length of the animal's body, such that tensile and compressive stresses coexist during dorso-ventral body bends. To perform proprioceptive activities as a response to compression and extension, mechanisms need to be in place to restrict spread of depolarization and confine the information locally. Under the notion of a high input resistance inherent to *C. elegans* neurons (*66*), a small input current during compression could, in principle, delocalize and depolarize the entire axon, hence disrupting the proprioceptive coordination along the length of the animal. DVA has several synapses along its length to each of the seven dorsal B-type motor neurons. Thus, the existence of a localized, dendritic output is supported by the wiring pattern. We propose that stretch activates TREK-2/TWK-16 and hence suppresses or at least dampens the NOMPC/TRP-4-related transduction current to achieve compartmentalized alternating "active zones" that correspond to the compressed state of the neurite (Fig. 8E). Such a mechanism would not only facilitate gain control during mechanical signaling subjected to stochastic ion channel noise but also allow to sample the full dynamic range of proprioceptor activity.

At least two alternative processes could plausibly explain the observed calcium increase during ventral bending: First, TRP-4 and TWK-16 could both be activated under mechanical tension during neurite extension on dorsal bends, but close with different kinetics. Under the assumption that TRP-4 closing kinetics are slower than TWK-16, they would remain open for a longer time and an apparent ventral activity is obtained. Our in vitro data showing that Ca^{2+} activity increased during tension relaxation can be interpreted as an argument against this scenario. Second, a single synapse from the ventral motor neurons to DVA has been described (*67*). This notion allows us to hypothesize that the ventral Ca^{2+} increases in DVA could be due to corollary discharge from VB motor neurons that provide a copy of the motor state to the central nervous system (*68*). Our data showing that DVA-specific mutations in *unc-70* lead to decorrelated Ca^{2+} dynamics contradicts this interpretation. However, whole animal Ca^{2+} imaging experiments are needed to further investigate and completely disprove this scenario.

In summary, our data revealed that compressive and tensile stresses modulate two opposing, excitatory and inhibitory ion channels of DVA proprioceptors, TRP-4 and TWK-16, respectively, and that spectrin interferes with proprioception of body postures. Our data point toward a general mechanism by which long mechanosensory dendrites achieve local computation through mechanical compartmentalization. Future experiments will need to directly address whether this result applies to other mechanosensory modalities and animals.

MATERIALS AND METHODS
Soft lithography and PDMS replica molding
SU-8 soft lithography and PDMS replica molding have been performed as described before (*69*). Briefly, the fabrication of the molds

was undertaken in-house as a single-layer process using standard SU-8 photolithography techniques. We first applied a 5-μm-thick adhesion layer to reduce liftoff of the patterned structure during device fabrication. Piranha cleaned 4-inch wafers were used to create an adhesion layer using SU-8 50 before photo patterning in SU-8 2000. After fabrication, molds were vapor phase–silanized in chlorotrimethylsilane to prevent adhesion of the PDMS to the substrate. A 10:1 mixture of Sylgard 184 prepolymer/curing agent was degassed (≈30 min in vacuum desiccator) and poured onto the silanized molds. After settling, the PDMS/wafer was baked at 80°C for 2 hours. Devices were then cut using a scalpel, lifted off, and punched with a biopsy punch (1 or 0.75 mm). The procedure of animal insertion into the trapping channel has been described in detail elsewhere (69). Briefly, to load individual in the chip, one young adult worm transgenic for TSMod in UNC-70 and its derivatives (GN517, GN519, GN600, and MSB233) (20) were picked from an NGM plate containing OP50 bacteria and transferred to a 5-μl droplet of 30% OptiPrep [to reduce scattering from PDMS due to refractive index mismatches between the animal and the surrounding (70, 71)] placed onto a hydrophobic substrate (25 cm² of Parafilm) to swim for 30 s and rid themselves from bacteria. Then, using a stereo dissecting scope at ×60 total magnification (Leica S80), the animals were aspirated into a 23-gauge metal tube (Phymep) connected to a 5-ml syringe (VWR) with a polyethylene (PE) tube (Phymep, BTPE-50; 0.58 mm by 0.97 mm) prefilled with 30% OptiPrep buffer. The loading tube was inserted in the inlet port of the device, while a gentle pressure onto the plunger of the syringe released the animals into WFS. Channel with a thickness of 60 μm was used to firmly hold animals immobile during the three-channel FRET imaging procedure without stretching or confining them visibly. After each image, the animals were pushed for a distance of π into the device to probe the opposite curvature at the samebody coordinate.

Animal maintenance
Animals were maintained using the standard protocols (72, 73) and grown at 20°C on nematode growth medium (NGM) plates with OP50 bacteria, unless indicated otherwise. For Gal4-expressing transgenes, animals were maintained and raised at 25°C to ensure consistent expression (32).

FRET imaging
Three-channel FRET imaging of animals transgenic for UNC-70(TSMod), UNC-70E2008K(TSMod), and no-force and high-FRET controls was carried out as described previously (20). The 2000-bp *unc-70* promoter fragment drives our *unc-70* cDNA predominantly in neurons, with little expression in muscles and no detectable expression in the hypodermis (fig. S6). Briefly, animals were either immobilized on agar pads (20) or in microfluidic chips with varying curvature as described above. Imaging was carried out on a Leica DMI6000 SP5 confocal microscope through a 63×/1.4 numerical aperture (NA) oil immersion lens. Three images were acquired: the direct donor (mTFP2) excitation and emission, donor excitation and acceptor emission, and the direct acceptor (mVenus) excitation and acceptor emission. mTFP2 was excited using the 458-nm, while mVenus was excited with the 514-nm line of an Argon ion laser at 80 and 11% transmission, respectively (with 25% of its full available power). The fluorescent light was collected using two hybrid GaAs avalanche photodiodes with 100% gain through an acousto-optical beam splitter with the donor emission window set between 465 and 500 nm and

the acceptor emission window set between 520 and 570 nm. Linearity of the detector and the ratio $\frac{\Psi_D}{\Psi_A}$ (ratio of collection efficiency of the two hybrid photodetectors (HyD)) was determined experimentally by imaging a homogeneous fluorescein solution with increasing gain at constant laser power. Each image was acquired as an average of four frames acquired at a 400-Hz line rate with 512 by 512 pixels at a digital zoom 3 (for fig. S6C) or zoom 1 to 1.5 (for Fig. 4 and fig. S6, E and G) in the microfluidic chip. For each imaging session, the donor→FRET bleedthrough and acceptor cross-excitation by the donor laser were determined using a sample with mTFP [ARM101 or MSB60; (74)] or mVenus (GN498) expression only, respectively (20). The bleedthrough and cross-excitation factor (alpha, delta) were calculated as described (20) and assumed to be constant across all intensities and images (for a given set of parameters). The raw FRET intensity I_F was then corrected according to

$$cF(i,j) = I_F(i,j) - \alpha \cdot I_A(i,j) - \delta \cdot I_D(i,j)$$

and the FRET efficiency E calculated using

$$E = 100 \cdot \frac{\left(cF \cdot Q_D \cdot \frac{\Psi_D}{\Psi_A}\right)}{qD + \left(cF \cdot Q_D \cdot \frac{\Psi_D}{\Psi_A}\right)}$$

For whole animal images in the WFS, collapsed maximum intensity projections from 15 images of a 3D stack undersampled with ≈2-μm interplane distance were background-subtracted with a constant value determined in a region of interest (ROI) that did not contain information from the animal. Before FRET calculation, the individual images were binned to 256 by 256 pixels to increase signal/noise ratio. For final display, the FRET map was overlaid on top of the corresponding bright-field (BF) image and displayed in Fig. 4 and fig. S6 (E and G). In contrast, individual neurons were traced using a Gaussian fit to the intensity profile and processed as described (20).

Neuron morphology imaging and analysis
Animals expressing mKate in DVA were embedded in the low percentage agar (1 to 2%), which allowed animals to undergo dorso-ventral body bends without moving out of field of view. Imaging was performed on a Leica DMi8 through a 40×/1.1 water immersion lens using the 575-nm line of a Lumencor SpectraX light-emitting diode (LED) light source. Fluorescence was collected through a 641/75-nm emission band-pass filter (Semrock, FF02-641/75-25) and recorded using a Hamamatsu Orca Flash 4 V3 for 1 to 2 min at 10 Hz with an exposure time of 50 ms. Out-of-focus frames were discarded, and the resulting videos were postprocessed as previously described (20).

Locomotion behavior analysis
Animal tracking platform and data acquisition
Animals were synchronized using standard alkaline hypochlorite (bleaching solution) treatment method. Arrested L1 were seeded onto OP50 NGM plates and incubated at 20°C. Without a lack of generality and to facilitate automated tracking and postprocessing, we recorded videos of the locomoting animals without food (OP50). To ensure that the absence of food did not alter the outcome of the experiment, we sampled the mutant genotypes and wt on food ($p_{off}^{N2-vs-CB524} = 3.4 \times 10^{-5}; p_{on}^{N2-vs-CB524} = 5.6 \times 10^{-4}$). Each video containing a single animal was 1 to 2 min in length and was taken at 25 frames/s. In total, ≈1 million frames were collected and processed

(table S1). Videos of the young adult animals were taken within 5 min after picking using a home-built animal behavior tracking platform. The custom build macroscope is composed of a scientific complementary metal-oxide semiconductor (sCMOS) camera (IDS UI-3080 CP Rev. 2) coupled to a Navitar 6.5× zoom lens at 2× zoom. A closed-loop stage tracking algorithm, implemented in C#, kept the animal in the field of view for the duration of the recording or was manually followed with a motorized *xz*-scanning stage (102 mm–by–102 mm travel; Standa), transilluminated with a diffused white light LED array (Thorlabs).

Auxin experiment and quantification of the knockdown

Auxin plates were prepared by adding 100 mM stock of 1-naphthaleneacetic acid (NAA; synthetic auxin; Sigma-Aldrich, 317918) dissolved in 100% ethanol to cooled NGM right before pouring the plates at a final concentration of 1 mM NAA (*30*). Once solidified, the auxin containing plates or only ethanol (1%) containing control plates were seeded with concentrated 10× OP50. Young adult animals containing TIR plasmid injected at 10 ng/μl were transferred to the auxin or control plates and incubated at room temperature (RT) for 2 hours before the video acquisition of their locomotion behavior.

Data analysis using eigenworms

Imaging processing was performed using custom MATLAB scripts based on (*22*) using the following methods:

1) All video frames were converted to grayscale images showing only the worm itself with a white background, which was achieved by background subtraction and two thresholding procedures.

a) Background subtraction. Each video was divided into several equal blocks. Then, a background image was created by taking the brightest pixel from the images, which was used to remove the background from the frames from that block.

b) First thresholding. After the background subtraction, the first threshold value was applied to the images that resulted in removal of most of the dark nonworm pixels.

c) Second thresholding. Subsequently, an adaptive thresholding, also known as Bradley method, was applied to remove the remaining small clutters, especially close to the worms.

2) Fast tracking pipeline, adapted from (*22*), was applied. Briefly, all frames were passed through the fast tracking pipeline; however, only simple (non–self-overlapping posture) frames were successfully processed but concurrently labeling the unprocessed frames as "crossed" (self-overlapping posture) frames that required further processing. The results from the tracking pipeline for the simple frames include the head/tail position, backbone, thickness, and modes (a_1, a_2, and a_3).

3) Crossed frames tracking.

a) Manual tracing. First, crossed frames were divided into a number of blocks where each block consists of continuous crossed frames. Then, each crossed block was downsampled at 5 Hz to perform manual annotation of the backbone.

b) Comparative reconstruction. For comparative reconstruction, we used either the first manually traced or the last image of the simple block (if any) to align with the first image of the crossed block using cross-correlation and to calculate the difference between the two images. Then, we applied the image thinning process to find the backbone of this difference. This backbone was then connected to the rest of the worm's backbone for that corresponding image. The comparative reconstruction step was repeated four times until the next manually traced frame. Now, the new manually traced frame

served as the reference for next four frames, and the process continued until the end of the crossed block. After the comparative reconstruction, we only got backbone of the worms; thus, we used the backbone to calculate the required modes (a_1, a_2, and a_3).

Calcium imaging and analysis
Imaging

Young adult animals were mounted onto 1 to 1.5% of agar pad with 3 to 5 μl of latex beads (Polybeads, 0.2 μm; Polysciences) to facilitate body movement and stabilize the position of field of view (*20*). Calcium imaging was performed using a Leica DMi8 microscope equipped with a 25×/0.95 water immersion lens, Lumencor SpectraX LED light source, and a Hamamatsu Orca Flash 4 V3 sCMOS camera. The GCaMP6s calcium sensor was excited with 30% of the cyan LED of the SpectraX with a 488-nm excitation filter (≈12 mW), and the calcium-insensitive signal was excited with the 50% of the green/yellow LED through a 575/25-nm excitation filter (≈33 mW) using a triple band-pass dichroic mirror in the filter turret (Semrock, FF409/493/596-Di02-25x36). The incident power of the excitation light was measured with a Thorlabs microscope slide power meter head (S170C) attached to PM101A power meter console. Emission was split with a Hamamatsu Gemini W-View with a 538-nm edge dichroic (Semrock, FF528-FDi1-25-36) and collected through two single-band emission filters, 512/25 nm for GCaMP (Semrock, FF01-512/25-25) and 670/30 nm for mKate (Semrock, FF01-670/30-25), respectively. Both emission signals were split onto top/bottom of the image sensor, enabling differential exposure times optimized for imaging. Individual frames were acquired at 10 Hz for 40 to 60 s (depending on worm movement) with an 88-ms and 50-ms exposure time, using the master pulse from the camera to trigger the light source through Hamamatsu HCImage software. Because it was impossible to resolve Ca^{2+} signals throughout the long DVA axon in moving animals, we restricted our curvature analysis to the posterior region close to the cell body.

For calcium imaging in the microfluidic WFS device, we first loaded individual animals into the curvature channel and immobilized them in a straight position. Then, we gently applied a pressure to that channel with the same loading syringe and pushed the animal, tailfirst, into the curved portion of the channel, while recording dual color fluorescent images at 10 Hz using the same imaging settings as for freely crawling animals described above. After the animal's tail passed through the bend, it was allowed to slide back into its original position. The procedure was repeated for dorsal and ventral bends.

Image analysis

Images were processed using custom built MATLAB routines to extract the mean intensity of the cell body as a function of body centerline curvature near the tail. Because of the omnipresent autofluorescent signal in the GFP channel, adaptive thresholding was able to separate the animal backbone from the background signal. First, the raw images from the GCaMP channel were binarized and eroded to find the skeleton of the worm in each frame. An iterative approach was chosen to prune the branches to get the longest path describing the centerline of the worm (*22*). Next, a segment of the centerline enough to capture one bend of the worm in the tail region was chosen, which was further divided into two equal segments using three points. These three points were used to construct a triangle and, subsequently, a circumcircle. Last, the curvature is calculated at the middle point of the three points using the radius of the circumcircle by the formula $\kappa = 1/R$, where R is the radius of the

circumcircle and κ is the curvature, and directionality of the curvature was determined by the sign of the tangential angle at the point where the curvature was calculated.

The neuron was labeled manually for the first frame in the mKate, calcium-insensitive channel, and automatically tracked in subsequent frames, based on a local search in the vicinity of the location in the previous frames. The area, position, and intensity were collected in the mKate channel, and its position was mapped onto the GCaMP channel to extract the intensity in each frame. Last, the calcium-sensitive signal was divided by the insensitive signal after background correction (for fig. S4, A and C) to obtain the ratio R that was normalized to the baseline ratio R_0. The trough of the periodic signals was taken as R_0. The background-subtracted calcium traces were divided by the background-subtracted mKate signal to yield the ratiometric intensity signal

$$ R = \frac{I^{Ca2+}(t) - I_{bg}^{Ca2+}(t)}{I^{mK8}(t) - I_{bg}^{mK8}(t)} $$

The fact that not all animals could be recorded with the same curvature change velocity and not all worms bent their bodies to the same extent precluded the calculation of an average calcium signal versus time. We thus transformed the periodic curvature c into a phase angle coordinate θ of 360° (52) along the ventral-dorsal-ventral bending trajectory according to

$$ \theta = \begin{cases} (c_{max} - c_t) \cdot \left(\dfrac{\pi}{c_{max} - c_{min}} \right) \text{ for } c' = \dfrac{\partial c}{\partial t} < 0 \\ 2\pi - (c_{max} - c_t) \cdot \left(\dfrac{\pi}{c_{max} - c_{min}} \right) \text{ for } c' = \dfrac{\partial c}{\partial t} > 0 \end{cases} $$

in which $c(t)$ is the curvature at a given point in time, c_{max} and c_{min} are the maximum curvature and minimum curvature, respectively, while c' is the first derivative of c with respect to time t. We arbitrarily assigned ventral to 0° and 360° (start and end of the cycle), while dorsal corresponded to 180°. The average calcium intensity ratio R/R_0 was calculated and plotted against the phase angle. A P value as a function of phase angle was calculated for indicated combinations of genotypes (fig. S9) according to standard procedures using a t test statistics $t = \frac{\bar{\mu}_1 - \mu_0}{\frac{s_1}{\sqrt{n_1}} + \frac{s_0}{\sqrt{n_0}}}$.

Molecular biology and transgenesis
Construction of CRE driver lines
To drive CRE expression in target neurons, we constructed plasmids carrying CRE recombinase (synthesized from Twist Bioscience) and $F49H12.4p$ for PVD (75), $nlp-12p$ for DVA (23), $acr-5p$ for B-type motor neurons (7), and $flp-22p\Delta 4p$ for SMD neurons (6). All promoters were amplified using primers as listed below from genomic DNA isolated from N2 wt laboratory strains and cloned into a vector carrying codon-optimized CRE (Twist Bioscience) and synthetic introns designed according to (76) terminated with a $tbb-2$ 3′ untranslated region (UTR) using Gibson assembly. All clones were verified by Sanger sequencing. $Nlp-12$p::CRE was injected at 1 ng/µl into N2 to yield MSB66, crossed to MSB115 [$unc-70(loxP)$], and integrated to yield mirIs71. The resulting strain was outcrossed two times and named MSB765. $acr-5$p::CRE was injected at 5 ng/µl into SV2049 and integrated to yield $mirIs37$ and outcrossed to obtain MSB510.

Generation of unc-70(flox) using CRISPR
CRISPR-Cas9 genome editing was performed using the previously described method with some modifications (77). Briefly, Cas9-crRNA-tracrRNA ribonucleoprotein complex together with the homology directed repair templates (HDR) was assembled in IDT Nuclease-Free Duplex Buffer [30 mM Hepes (pH 7.5) and 100 mM potassium acetate] and Milli-Q water. As in the co-CRISPR method, we coinjected Cas9 complexes and repair templates targeting the marker gene $dpy-10$ to incorporate the semidominant $cn64$ allele. Twenty to 30 young adult hermaphrodites were injected with the injection mix containing Cas9-crRNA-tracrRNA-HDR and recovered onto individual plates. In some cases, more than one crRNA were used. After 3 days after injection, successful edits were identified on the basis of the dominant $dpy-10(cn64)$ roller phenotype and picked to individual plates to produce self-progeny. Mothers were then lysed and screened by polymerase chain reaction (PCR) for the corresponding edits. To generate the final genotypes, the CRE driver strains were bred with EG7944 (78) to mark the position of $unc-70$ on chromosome 5 before crossing into $unc-70$ floxed strain to establish the cell-specific CRE in the $unc-70$(floxed) background. Successful recombination of the $unc-70$ locus was confirmed by PCR.

Generation of GFP::TRP-4 using CRISPR
Insertion of GFP at the N terminus of TRP-4 was performed using the two-step nested CRISPR method (38). First, parts of GFP(1 and 3) along with a flexible linker were inserted at the N-terminal genomic locus of $trp-4$ using the crRNA, and the 200-bp single-stranded oligodesoxynucleotide (ssODN) indicated in the CRISPR reagents (table S4). This fragment also contained a new protospacer adjacent motif (PAM) site and a protospacer sequence that, in step 2, allowed the in-frame insertion of the remaining sequence of 700 bp (GFP2) of GFP. In step 2, the same universal crRNA (see CRISPR reagents; table S4) mentioned in (38) was used to make the double-strand break, and for the repair template, IDT gblock was used. The correct in-frame insertion of full-length GFP was sequence verified.

Expression of TRP-4 in TRNs
The $mec-4$ promoter was amplified from pMH686 [gift of M. Harterink (79)] and cloned together using Gibson assembly with synthetic cDNA fragments produced by Twist Bioscience, containing full-length TRP-4 (residues 1 to 1924) or truncated TRP-4 lacking the N-terminal domain with the ankyrin repeats (residues 1433 to 1924) to yield pNM2. The resulting plasmids were injected at 20 ng/µl into GN692 (80) to yield MSB382 and MSB379, respectively.

Rescue of TRP-4 specifically in DVA
The $nlp-12$ promoter was amplified from pRD1 and cloned together using Gibson assembly with synthetic cDNA fragment containing full-length TRP-4 (Twist Bioscience) amplified from pNM2 to yield pRD21. The resulting plasmid was injected at 50 ng/µl into MSB387 to yield MSB706 ($mirEx280$[nlp-12p::TRP-4cDNA; myo-2p::mCherry]). $mirEx280$ was integrated to yield $mirIs89$ and was outcrossed to obtain MSB728.

DVA-specific rescue of unc-70
The $nlp-12$ promoter was amplified from pRD14 and cloned together using Gibson assembly with $unc-70$ cDNA fragments amplified from pMK93 ($unc-70$p::$unc-70$cDNA::$unc-54$-3′UTR) to yield pRD22. The resulting plasmid was injected at 20 ng/µl into MSB188.

Generation of mutant TWK-16 allele
Conditional allele
We tagged $twk-16$ locus directly after the first ATG with worm optimized mScarlet, wScarlet, and a degron tag borrowed from the

AID system, using SunyBiotech's CRISPR services. We could identify wScarlet::TWK-16 expression in a single neuron in the tail (DVA) and two neurons in the head (probably, AVK and ADE). The fusion of TWK-16 with the AID::wScarlet tag did not cause any locomotion defects as compared to wt worms (fig. S8, E to G), indicating full functionality of the transgene.

Constitutive mutation

We removed 1672 bp from the genomic locus of *twk-16*, the region spanning the first two exons and the intron in between them. Two crRNAs were used to cut right before the start codon and in the intron region after the second exon, with a donor consisting of an ssODN containing the two 35-bp homology arms, flanking the PAM sequence of the two crRNAs.

DVA-Gal4 driver

The DVA-Gal4 driver was constructed using Gibson assembly of the backbone amplified from pHW393 [*rab-3p::GAL4-SK(DBD)::VP64::let-858* 3′UTR, Addgene, plasmid #85583] (*32*) and insert fragment containing *nlp-12p* amplified from pRD1 (*nlp-12p::CRE::tbb-2* 3′UTR) plasmid to yield pRD10. The resulting plasmid was injected at 5 ng/μl together with *unc-122p::mCherry* as coinjection marker and integrated by ultraviolet (UV) irradiation using standard procedures.

DVA and TRN::TIR driver

The TRN-TIR driver was constructed using Gibson assembly of the backbone amplified from pUN1020 [*fln-1p::TIR::F2A::mCherry::H2B*, a gift from the Cram laboratory (*31*)] and insert fragment containing *mec-4p* amplified from pNM2 (*mec-4p::TRP-4::tbb-2* 3′UTR) plasmid to yield pNS30. The resulting plasmid was injected at 30 ng/μl together with *unc-122p:mCherry* as coinjection marker. The DVA-TIR driver was constructed using Gibson assembly of the backbone amplified from pNS30 and insert fragment containing *nlp-12p* amplified from pRD1 plasmid to yield pNS43. The resulting plasmid was injected at 10 ng/μl together with *unc-122p:mCherry* as coinjection marker.

Generation of the E2008K allele in UNC-70(TSMod)

pRD7 was constructed using Gibson assembly of the backbone amplified from pMK35(*pExprunc-70R8TSmodR9::unc-54* 3′UTR) and insert synthetic fragment (Twist Bioscience) containing E2008K mutation. The resulting plasmid was injected at 20 ng/μl.

Extrachromosomal array and integration

Extrachromosal arrays were generated by injecting the aforementioned amount of DNA into the appropriate strain and selecting for the F1 progenies with the coinjection marker. Three independent lines were generated whenever possible. The integration of the extrachromosomal array was performed using UV/trimethylpsoralen (TMP) method. Briefly, late L4 young adult animals carrying the array were picked onto an NGM plate without OP50. These animals were fed trimethylpsoralen (TMP, SigmaAldrich) TMP at a final concentration of 50 μg/ml for 20 min. Then, they were UV-irradiated for 30 s at 4.5 mW/cm^2 (250nm peak wavelength; ~130mJ) and expanded for 3 to 4 weeks before selection. Three independent integrated lines were recovered whenever possible.

Primary culture and mechanical stimulation
DVA primary cell culture

Embryonic cell isolation was performed using a previously described method with some modifications (*20*). Briefly, synchronized worms seeded onto peptone-enriched plates and incubated at RT until the plates were populated with eggs. Then, the plates were washed off, and the eggs were collected using Milli-Q H_2O. The worm and egg pellets were resuspended in the freshly prepared bleaching solution and rocked gently for 4 to 7 min, once 70 to 80% of the worms were lysed the reaction was stopped using egg buffer [118 mM NaCl, 48 mM KCl, 2 mM $CaCl_2$, 2 mM $MgCl_2$, 25 mM Hepes (pH 7.3), and an osmolarity of 340 mosM]. The collected eggs were washed three times with fresh egg buffer. Then, the eggs were separated using 30% final concentration of sucrose by centrifuging at 1200 rpm for 20 min. The separated top layers of eggs were collected in a new tube and washed two to three times with egg buffer. Then, the eggs were treated with chitinase (0.5 U/ml) for 40 min to dissociate embryonic cells. The chitinase reaction was stopped using L15 medium. After chitinase treatment, the embryos with the digested egg cells were passed through 25-gauge needle 10 to 15 times for dissociating into single cells. The dissociated cell suspension was filtered through 5-μm Durapore filter (Millipore). Then, the single-cell solution was centrifuged for 3 min at 3200 rpm, and the pellet was resuspended in L15 medium.

Optical trapping chambers were based on two parallel glass surfaces spaced with a 50-μm-thick PDMS layer (1:10 curing agent; Sylgard). A glass bottom petri dish (BD, Wilco Glass, #1.5) was spin-coated for 1 min at 750 rpm (*81*) and cured for 1 hour at 65°C. A 1 cm–by–1 cm square cavity was gently peeled off with a scalpel, and the bottom dishes were then sterilized by UV irradiation for 1 hour. The cavity was then incubated with a 100-μl drop of peanut lectin (Medicago, Sweden) diluted 1:10 into phosphate-buffered saline (PBS) for 20 min. After that, the plate was rinsed with L15 medium, and a 150-μl drop containing the cells was seeded. Cell density was 1.5×10^5 mL^{-1} to ensure enough number of DVA neurons per plate, while keeping and appropriate space for the tether extrusion experiments. After 60 min, 0.5 ml of L15 medium was added and the cells were cultured at 25°C overnight. Fresh medium was changed (0.5 to 1 ml) every 24 hours. All experiments were carried out between 1 and 4 days after isolation.

Stimulation of DVA neurons cultured on elastic substrates

For the axonal deformation experiments, the neurons were directly seeded on the PDMS surface. The latter was obtained by spin-coating a bottom glass (Wilco Glass, #1.5) for 1 min at 750 rpm. The coated dish was then plasma-treated for 5 min (Plasma Surface Technology, Diener Electronic), UV-irradiated for 1 hour, and incubated with 500 μl of peanut lectin (1:10 in PBS; Sigma-Aldrich) for 24 hours. Axonal deformation was undertaken by indentation of the substrate with a 1-mm-thick microinjection needle held with a 4D control micromanipulator (uMP-4, Sensapex). The needle tip was brought ≈5 μm away from the axonal tip and pushed vertically to induce substrate indentation. Substrate deformation was determined from the average perpendicular displacement at the middle of the axon. GCaMP activity was measured from the cell body and was normalized to the mKate, Ca^{2+}-independent fluorescence signal (see below). A total of 25 cells were tested, 18 of which showed reproducible responses to substrate indentation.

Optical measurement of membrane mechanics and calcium activity

The optical tweezer (OT) platform (SENSOCELL, IMPETUX OPTICS, Spain) consists of a continuous wave laser (λ = 1064 nm, 5-W nominal output power; Azur Light) steered with a pair of acousto-optic deflectors (AOD1 and AOD2) and a force detection

module that captures the forward-scattered light from the optical traps (fig. S7A). This is mounted around an inverted research microscope (Nikon Eclipse Ti2) equipped with a spinning disk confocal microscope (Andor DragonFly 502, Oxford Instruments) on top of an active isolation table (Newport). The laser is directed onto a microscope objective (MO; 60×/NA = 1.2; water immersion, Nikon) after being expanded with a telescope (lenses L1 and L2) to fill the MO entrance pupil, through the epifluorescence port. A short-pass dichroic mirror (D1) reflects the infrared (IR) trapping beam and transmits both the excitation and emission light for fluorescence microscopy, as well as BF illumination. To prevent from IR light leaking toward the detector, a neutral, shortpass filter (IR-F) was placed at the imaging optical path. The optical traps were positioned using LightAce software (IMPETUX OPTICS, Spain), in synchronization with a CMOS camera (BlackFly S, FLIR Systems), recording BF images of the sample. The force detection module of our OT platform operates by detecting light-momentum changes, after capturing the scattered trapping beam through an NA of 1.4, oil immersion collecting lens, with a position-sensitive detector (PSD) placed at plane optically equivalent to the back focal plane (BFP) (82). This allowed us to measure forces with no previous trap calibration and beyond the linear trapping regime, thus covering the full spectrum until the escape force of ≈200 pN, hence allowing working with lower laser power (250 mW), as compared to standard BFP interferometry (82). The module enables the BF illumination to pass through, which is properly filtered to avoid leakage into the PSD.

Membrane tether extrusion

Before force measurements, red fluorescent, 1-μm polystyrene microspheres (FluoSpheres F8816, Thermo Fisher Scientific) were washed with cell culture medium by centrifuging at 10^4 rpm for 3 min and added to the sample chambers at a concentration of 2×10^5 μl^{-1} and was then covered with a 25 mm-by-25 mm cover glass (#1.5, Ted Pella). The microspheres were captured in a 250-mW optical trap (laser power at the sample plane) and brought close to a DVA neuronal axon for 1 s before retraction to produce a stable membrane tether. The tethering force, F_{tether}, was balanced with the trapping force, F_{OT}, resulting in a change in the trapping beam momentum detected with the force detection module. Pulling routines were predefined with LightAce software (IMPETUX OPTICS) as follows (Fig. 6G). First, the bead was brought into contact with the axon and pulled a distance of 10 μm, reaching a peak in the tether tension value. Second, the bead stopped for 10 s, letting the tether tension to relax down to a static value arising from the stored stress. Third, the bead was brought back to the initial position and held at a constant position again for 10 s. This routine was repeated three times for every DVA neuron tested at increasing velocities, 5, 20, and 80 μm/s. Last, every force measurement was compensated for initial momentum variation by subtracting a baseline trajectory taken on the same positions without a bead. The appearance of the Ca^{2+} transients is likely caused by the mechanical perturbation as opposed to local heating, as tether-free trials were unable to elicit reproducible changes (fig. S7, C and D). During each tether extrusion sequence, GCaMP and mKate fluorophores were simultaneously excited using the 488- and 561-nm laser lines of an Andor DragonFly spinning disk confocal microscope, respectively. The excitation beam is corrected for nonuniformity and throughput using a Borealis Illuminator (Andor, Oxford Instruments), before it passes through a quad band dichroic mirror (D2, 405, 488, 561, and 637 nm,

Andor). After illuminating the sample plane, fluorescence emission is reflected at D2 and split with a 565-nm longpass dichroic mirror (D3) to image GCaMP and mKate emissions using F1: λ = 521 nm and F2: λ = 647 nm at two identical, back-illuminated sCMOS cameras (sCMOS1 and sCMOS2, Andor, Oxford Instruments).

Data analysis of tether pulling

Peak (F_{peak}) and storing (F_{base}) force values were obtained from the trapping force signals during the tether extrusion experiments (fig. S7B). Tension was calculated from the force according to (40). GCaMP emission was measured both from the cell body and tether neck by setting an ROI with Fiji (83). The background contribution was measured far from the neuron and subtracted from the intensity profile. The photobleaching trend was corrected by normalization over an exponential fit, providing the background-subtracted and baseline-normalized GCaMP signal (F/F_0). Tension-modulated calcium activity was observed in ≈30% of all extrusion events and is thus within the single-molecule approximation (84). To determine whether the changes in neuronal membrane tension induced a significant increment in the GCaMP intensity, this was measured for a 3-s time frame before and after the tether was extruded. Because the two synchronized cameras recorded videos with a 10-frame rate, GCaMP intensity values were averaged over N = 30 data points. The two intensity values (before and after pulling) were t-tested and thresholded within a P < 0.01. When significant, the pulling events were classified into GCaMP-increasing ($\Delta I > 5\%$) and GCaMP-decreasing ($\Delta I < 5\%$). To rule out that the Ca^{2+} transient was caused by heating of the trapping laser, we carried out a series of measurements on wt DVA neurons in the absence of a membrane nanotube, tethering the trapped microbead and the neuronal axon (without prior contact of the bead).

Neuromechanical model

Without exception, all parameters and assumptions have been reproduced as outlined in (48). Briefly, the framework consists of a 2D structural skeleton composed of 46 segments and 98 discrete joints distributed on the ventral and dorsal sides. These joints are vertically connected by incompressible rods and lateral connections embody passive forces modeled as a Kelvin-Voigt material with a spring and a dashpot in parallel, owing a constant material property. Diagonal elements, connecting neighboring joints on opposing sides, represent the effect of pressure and ensure volume conservation. In parallel to the passive force, "muscle" forces are computed as an active Kelvin-Voigt material with varying spring constants and viscosities, whose parameters are slaved to neuronal state variable of the motor circuit (active and inactive). For details, see (48).

The minimal motor circuit was embedded into that active/ passive framework, consisting of a pair of excitatory (DB and VB) and inhibitory motor neurons (DD and VD). The current within the motor ventral motor circuit has contribution from stretch receptors, in addition to the input current from AVB and motor current driving muscle actuators. The current in dorsal motor neuron does not contain adjustments from the stretch receptor. We modified the model according to our experimental data: We eliminated dorsal stretch receptor currents $\frac{\partial I}{\partial \epsilon} = 0$ (with $\epsilon = dc$ as the strain) and inverted the relationship of the stretch receptor current on the ventral side and deliver it to B-class motor neurons on the dorsal side. No other stretch receptors were considered on the ventral side. In this model, a compression on the ventral side generates a polarizing response, which results in polarizing current flowing into the

B-class motor neurons on the dorsal side, and vice versa, the stretch on the ventral side generates a hyperpolarizing response. The DVA neuron is implemented indirectly, as a compression/stretch sensor, sending either positive or negative current to DB neurons. (A similar effect can be achieved by modifying the firing rate of DVA, which is nonzero at resting length.) The factor modifying the effective stretch receptor activation function (−**S**) was implemented in the original [equation 11 in (*48*)]

$$h_{\mathrm{m}}^{\mathrm{k}} = -\mathbf{S}\,\lambda_{\mathrm{m}}\gamma_{\mathrm{m}}^{\mathrm{k}}\frac{L_{\mathrm{L,m}}^{\mathrm{k}} - L_{\mathrm{0L,m}}}{L_{\mathrm{0L,m}}} \tag{1}$$

where **S** scales the effective stretch receptor activation function. This may be understood as decreasing the number of effective stretch/compression-sensitive ion channels or a failure to recruit active ion channels (equivalent to a failure in force transmission).

Statistics

Statistical analyses were performed in R and Igor. To construct and visualize the 3D distributions of the modes (a_1, a_2, and a_3), the 3D kernel density estimate of the first three modes was calculated in R using the ks package (*85*) with an unconstrained plug-in selector bandwidth. We choose to indicate the 10, 25, and 50% contours of the highest density regions in the manifold and the 2D projections of the floating data cloud along the corresponding planes. To compare two different datasets and test for the null hypothesis that the two kernel density functions are similar, we resampled the highly oversampled population by bootstrapping to avoid spurious significance due to long tailed outliers. The resampling and testing were performed 1000 times to yield a distribution of P values, which is displayed as a violin plot summarizing each figure of locomotion data. The resampling does not lead to significant discrimination of the downsampled and original dataset within the same population. Alternatively, the local density between two distributions was tested using a binned kernel density estimator. For this, we used the kde.local.test function from the ks package in R (*85*) to (i) convert all n data points of each distribution to counts on a 100 by 100 by 100 binning grid and embedded into a matrix C, (ii) evaluate the kernel function at these grid points to embed them into a matrix K, and (iii) then obtain the binned density estimator f from a sequence of discrete convolutions of C and K. The exact formulation of that procedure and a detailed presentation of the algorithm can be found in (*86*). For all grid points in which $P>0.01$, we accept the null hypothesis that the two densities at this grid point for the two distributions are the same. For all other grid points, a polarity is assigned and plotted as two different colors in a 3D voxelgram (e.g., Fig. 1D), indicating that $x1 > x2$ or $x1 < x2$. Swarm plots and estimation statistics have been calculated using the methods described in (*87*).

SUPPLEMENTARY MATERIALS

Supplementary material for this article is available at https://science.org/doi/10.1126/sciadv.abg4617

View/request a protocol for this paper from *Bio-protocol*.

REFERENCES AND NOTES

1. J. Gjorgjieva, D. Biron, G. Haspel, Neurobiology of *Caenorhabditis elegans* locomotion: Where do we stand? *Bioscience* **64**, 476–486 (2014).
2. N. A. Croll, Behavioural analyses of nematode movement. *Adv. Parasitol.* **13**, 71–122 (1975).
3. U. Proske, S. C. Gandevia, The proprioceptive senses: Their roles in signaling body shape, body position and movement, and muscle force. *Physiol. Rev.* **92**, 1651–1697 (2012).
4. W. Li, Z. Feng, P. W. Sternberg, X. Z. Shawn Xu, A *C. elegans* stretch receptor neuron revealed by a mechanosensitive TRP channel homologue. *Nature* **440**, 684–687 (2006).
5. L. Tao, D. Porto, Z. Li, S. Fechner, S. A. Lee, M. B. Goodman, X. Z. S. Xu, H. Lu, K. Shen, Parallel processing of two mechanosensory modalities by a single neuron in *C. elegans*. *Dev. Cell* **51**, 617–631.e3 (2019).
6. J. Yeon, J. Kim, D.-Y. Kim, H. Kim, J. Kim, E. J. du, K.-J. Kang, H.-H. Lim, D. Moon, K. Kim, A sensory-motor neuron type mediates proprioceptive coordination of steering in *C. elegans* via two TRPC channels. *PLOS Biol.* **16**, e2004929 (2018).
7. Q. Wen, M. D. Po, E. Hulme, S. Chen, X. Liu, S. W. Kwok, M. Gershow, A. M. Leifer, V. Butler, C. Fang-Yen, T. Kawano, W. R. Schafer, G. Whitesides, M. Wyart, D. B. Chklovskii, M. Zhen, A. D. T. Samuel, Proprioceptive coupling within motor neurons drives *C. elegans* forward locomotion. *Neuron* **76**, 750–761 (2012).
8. P. Liu, B. Chen, Z.-W. Wang, GABAergic motor neurons bias locomotor decision-making in *C. elegans*. *Nat. Commun.* **11**, 5076 (2020).
9. W. R. Schafer, Mechanosensory molecules and circuits in *C. elegans*. *Pflugers Arch.* **467**, 39–48 (2014).
10. R. Das, S. Wieser, M. Krieg, Neuronal stretch reception – Making sense of the mechanosense. *Exp. Cell Res.* **378**, 104–112 (2019).
11. B. D. Umans, S. D. Liberles, Neural sensing of organ volume. *Trends Neurosci.* **41**, 911–924 (2018).
12. S.-H. Woo, V. Lukacs, J. C. de Nooij, D. Zaytseva, C. R. Criddle, A. Francisco, T. M. Jessell, K. A. Wilkinson, A. Patapoutian, Piezo2 is the principal mechanotransduction channel for proprioception. *Nat. Neurosci.* **18**, 1756–1762 (2015).
13. S. H. Lin, Y. R. Cheng, R. W. Banks, M. Y. Min, G. S. Bewick, C. C. Chen, Evidence for the involvement of ASIC3 in sensory mechanotransduction in proprioceptors. *Nat. Commun.* **7**, 11460 (2016).
14. P. Jin, D. Bulkley, Y. Guo, W. Zhang, Z. Guo, W. Huynh, S. Wu, S. Meltzer, T. Cheng, L. Y. Jan, Y.-N. Jan, Y. Cheng, Electron cryo-microscopy structure of the mechanotransduction channel NOMPC. *Nature* **547**, 118–122 (2017).
15. P. Jin, L. Y. Jan, Y.-N. Jan, Mechanosensitive ion channels: Structural features relevant to mechanotransduction mechanisms. *Annu. Rev. Neurosci.* **43**, 207–229 (2020).
16. D. Argudo, S. Capponi, N. P. Bethel, M. Grabe, A multiscale model of mechanotransduction by the ankyrin chains of the NOMPC channel. *J. Gen. Physiol.* **151**, 316–327 (2019).
17. Y. Wang, Y. Guo, G. Li, C. Liu, L. Wang, A. Zhang, Z. Yan, C. Song, The push-to-open mechanism of the tethered mechanosensitive ion channel NOMPC. *eLife* **10**, e58388 (2021).
18. S. G. Brohawn, How ion channels sense mechanical force: Insights from mechanosensitive K2P channels TRAAK, TREK1, and TREK2. *Ann. N. Y. Acad. Sci.* **1352**, 20–32 (2015).
19. J. M. Kefauver, A. B. Ward, A. Patapoutian, Discoveries in structure and physiology of mechanically activated ion channels. *Nature* **587**, 567–576 (2020).
20. M. Krieg, A. R. Dunn, M. B. Goodman, Mechanical control of the sense of touch by β-spectrin. *Nat. Cell Biol.* **16**, 224–233 (2014).
21. G. J. Stephens, B. Johnson-Kerner, W. Bialek, W. S. Ryu, Dimensionality and dynamics in the behavior of *C. elegans*. *PLOS Comput. Biol.* **4**, e1000028 (2008).
22. O. D. Broekmans, J. B. Rodgers, W. S. Ryu, G. J. Stephens, Resolving coiled shapes reveals new reorientation behaviors in *C. elegans*. *eLife* **5**, e17227 (2016).
23. I. Hums, J. Riedl, F. Mende, S. Kato, H. S. Kaplan, R. Latham, M. Sonntag, L. Traunmüller, M. Zimmer, Regulation of two motor patterns enables the gradual adjustment of locomotion strategy in *Caenorhabditis elegans*. *eLife* **5**, e14116 (2016).
24. S. Moorthy, L. Chen, V. Bennett, *Caenorhabditis elegans* β-G spectrin is dispensable for establishment of epithelial polarity, but essential for muscular and neuronal function. *J. Cell Biol.* **149**, 915–930 (2000).
25. M. Hammarlund, W. S. Davis, E. M. Jorgensen, Mutations in β-spectrin disrupt axon outgrowth and sarcomere structure. *J. Cell Biol.* **149**, 931–942 (2000).
26. S. Ruijtenberg, S. Van Den Heuvel, G1/S inhibitors and the SWI/SNF complex control cell-cycle exit during muscle differentiation. *Cell* **162**, 300–313 (2015).
27. E. Kage-Nakadai, R. Imae, Y. Suehiro, S. Yoshina, S. Hori, S. Mitani, A conditional knockout toolkit for *Caenorhabditis elegans* based on the Cre/loxP recombination. *PLOS ONE* **9**, e114680 (2014).
28. Z. Hu, E. C. G. Pym, K. Babu, A. B. Vashlishan Murray, J. M. Kaplan, A neuropeptide-mediated stretch response links muscle contraction to changes in neurotransmitter release. *Neuron* **71**, 92–102 (2011).
29. L. Zhang, J. D. Ward, Z. Cheng, A. F. Dernburg, The auxin-inducible degradation (AID) system enables versatile conditional protein depletion in *C. elegans*. *Development (Cambridge)* **142**, 4374–4384 (2015).
30. M. A. Q. Martinez, B. A. Kinney, T. N. Medwig-Kinney, G. Ashley, J. M. Ragle, L. Johnson, J. Aguilera, C. M. Hammell, J. D. Ward, D. Q. Matus, Rapid degradation of *Caenorhabditis*

elegans proteins at single-cell resolution with a synthetic auxin. *G3 (Bethesda)* **10**, 267–280 (2019).

31. A. C. E. Wirshing, E. J. Cram, Spectrin regulates cell contractility through production and maintenance of actin bundles in the *Caenorhabditis elegans* spermatheca. *Mol. Biol. Cell* **29**, 2433–2449 (2018).

32. H. Wang, J. Liu, S. Gharib, C. M. Chai, E. M. Schwarz, N. Pokala, P. W. Sternberg, cGAL, a temperature-robust GAL4-UAS system for *Caenorhabditis elegans*. *Nat. Methods* **14**, 145–148 (2016).

33. S. R. Lockery, K. J. Lawton, J. C. Doll, S. Faumont, S. M. Coulthard, T. R. Thiele, N. Chronis, K. E. McCormick, M. B. Goodman, B. L. Pruitt, Artificial dirt: Microfluidic substrates for nematode neurobiology and behavior. *J. Neurophysiol.* **99**, 3136–3143 (2008).

34. M. Krieg, J. Stühmer, J. G. Cueva, R. Fetter, K. Spilker, D. Cremers, K. Shen, A. R. Dunn, M. B. Goodman, Genetic defects in β-spectrin and tau sensitize *C. elegans* axons to movement-induced damage via torque-tension coupling. *eLife* **6**, e20172 (2017).

35. M. Krieg, A. R. Dunn, M. B. Goodman, Mechanical systems biology of *C. elegans* touch sensation. *Bioessays* **37**, 335–344 (2015).

36. O. A. Bauchau, J. I. Craig, Euler-Bernoulli beam theory, in *Structural Analysis*, O. A. Bauchau, J. I. Craig, Eds. (Springer, 2009), pp. 173–221.

37. C. Grashoff, B. D. Hoffman, M. D. Brenner, R. Zhou, M. Parsons, M. T. Yang, M. A. McLean, S. G. Sligar, C. S. Chen, T. Ha, M. A. Schwartz, Measuring mechanical tension across vinculin reveals regulation of focal adhesion dynamics. *Nature* **466**, 263–266 (2010).

38. J. Vicencio, C. Martínez-Fernández, X. Serrat, J. Cerón, Efficient generation of endogenous fluorescent reporters by nested CRISPR in *Caenorhabditis elegans*. *Genetics* **211**, 1143–1154 (2019).

39. D. Lockhead, E. M. Schwarz, R. O'Hagan, S. Bellotti, M. Krieg, M. M. Barr, A. R. Dunn, P. W. Sternberg, M. B. Goodman, The tubulin repertoire of *Caenorhabditis elegans* sensory neurons and its context-dependent role in process outgrowth. *Mol. Biol. Cell* **27**, 3717–3728 (2016).

40. F. M. Hochmuth, J. Y. Shao, J. Dai, M. P. Sheetz, Deformation and flow of membrane into tethers extracted from neuronal growth cones. *Biophys. J.* **70**, 358–369 (1996).

41. A. Nekouzadeh, Y. Rudy, Statistical properties of ion channel records. Part I: Relationship to the macroscopic current. *Math. Biosci.* **210**, 291–314 (2007).

42. G. I. Bell, Models for the specific adhesion of cells to cells. *Science* **200**, 618–627 (1978).

43. L. Kang, J. Gao, W. R. Schafer, Z. Xie, X. Z. S. Xu, *C. elegans* TRP family protein TRP-4 is a pore-forming subunit of a native mechanotransduction channel. *Neuron* **67**, 381–391 (2010).

44. L. Salkoff, A. Butler, G. Fawcett, M. Kunkel, C. McArdle, G. Paz-y-mino, N. Nonet, N. Walton, Z. W. Wang, A. Yuan, A. Wei, Evolution tunes the excitability of individual neurons. *Neuroscience* **103**, 853–859 (2001).

45. C. Puckett Robinson, E. M. Schwarz, P. W. Sternberg, Identification of DVA interneuron regulatory sequences in *Caenorhabditis elegans*. *PLOS ONE* **8**, e54971 (2013).

46. S. G. Brohawn, Z. Su, R. MacKinnon, Mechanosensitivity is mediated directly by the lipid membrane in TRAAK and TREK1 K$^+$ channels. *Proc. Natl. Acad. Sci. U.S.A.* **111**, 3614–3619 (2014).

47. E. Schiksnis, A. L. Nicholson, M. S. Modena, M. N. Pule, J. A. Arribere, A. E. Pasquinelli, Auxin-independent depletion of degron-tagged proteins by TIR1. *microPublication Biol.* **2020**, 3 (2020).

48. J. H. Boyle, S. Berri, N. Cohen, Gait modulation in *C. elegans*: An integrated neuromechanical model. *Front. Comput. Neurosci.* **6**, 10 (2012).

49. L. R. Varshney, B. L. Chen, E. Paniagua, D. H. Hall, D. B. Chklovskii, Structural properties of the *Caenorhabditis elegans* neuronal network. *PLoS Comput. Biol.* **7**, e1001066 (2011).

50. D. Witvliet, B. Mulcahy, J. K. Mitchell, Y. Meirovitch, D. R. Berger, Y. Wu, Y. Liu, W. X. Koh, R. Parvathala, D. Holmyard, R. L. Schalek, N. Shavit, A. D. Chisholm, J. W. Lichtman, A. D. T. Samuel, M. Zhen, Connectomes across development reveal principles of brain maturation. *Nature* **596**, 257–261 (2020).

51. M. Kelley, J. Yochem, M. Krieg, A. Calixto, M. G. Heiman, A. Kuzmanov, V. Meli, M. Chalfie, M. B. Goodman, S. Shaham, A. Frand, D. S. Fay, FBN-1, a fibrillin-related protein, is required for resistance of the epidermis to mechanical deformation during *C. elegans* embryogenesis. *eLife* **4**, e06565 (2015).

52. L. He, S. Gulyanon, M. Mihovilovic Skanata, D. Karagyozov, E. S. Heckscher, M. Krieg, G. Tsechpenakis, M. Gershow, W. D. Tracey Jr., Direction selectivity in drosophila proprioceptors requires the mechanosensory channel Tmc. *Curr. Biol.* **29**, 945–956.e3 (2019).

53. M. Prager-Khoutorsky, A. Khoutorsky, C. Bourque, Unique interweaved microtubule scaffold mediates osmosensory transduction via physical interaction with TRPV1. *Neuron* **83**, 866–878 (2014).

54. A. Hassan, L. Sapir, I. Nitsan, R. T. Greenblatt Ben-el, N. Halachmi, A. Salzberg, S. Tzlil, A change in ECM composition affects sensory organ mechanics and function. *Cell Rep.* **27**, 2272–2280.e4 (2019).

55. X. Liang, J. Madrid, R. Gärtner, J.-M. Verbavatz, C. Schiklenk, M. Wilsch-Bräuninger, A. Bogdanova, F. Stenger, A. Voigt, J. Howard, A NOMPC-dependent membrane-microtubule connector is a candidate for the gating spring in fly mechanoreceptors. *Curr. Biol.* **23**, 755–763 (2013).

56. W. Zhang, L. E. Cheng, M. Kittelmann, J. Li, M. Petkovic, T. Cheng, P. Jin, Z. Guo, M. C. Göpfert, L. Y. Jan, Y. N. Jan, Ankyrin repeats convey force to gate the NOMPC mechanotransduction channel. *Cell* **162**, 1391–1403 (2015).

57. J. Howard, S. Bechstedt, Hypothesis: A helix of ankyrin repeats of the NOMPC-TRP ion channel is the gating spring of mechanoreceptors. *Curr. Biol.* **14**, R224–R226 (2004).

58. Y. A. Nikolaev, C. D. Cox, P. Ridone, P. R. Rohde, J. F. Cordero-Morales, V. Vásquez, D. R. Laver, B. Martinac, Mammalian TRP ion channels are insensitive to membrane stretch. *J. Cell Sci.* **132**, jcs238360 (2019).

59. Y.-C. Lin, Y. R. Guo, A. Miyagi, J. Levring, R. M. Kinnon, S. Scheuring, Force-induced conformational changes in PIEZO1. *Nature* **573**, 230–234 (2019).

60. J. M.-J. Romac, R. A. Shahid, S. M. Swain, S. R. Vigna, R. A. Liddle, Piezo1 is a mechanically activated ion channel and mediates pressure induced pancreatitis. *Nat. Commun.* **9**, 1715 (2018).

61. N. Srivastava, D. Traynor, M. Piel, A. J. Kabla, R. R. Kay, Pressure sensing through Piezo channels controls whether cells migrate with blebs or pseudopods. *Proc. Natl. Acad. Sci. U.S.A.* **117**, 2506–2512 (2020).

62. S. R. Taylor, G. Santpere, A. Weinreb, A. Barrett, M. B. Reilly, C. Xu, E. Varol, P. Oikonomou, L. Glenwinkel, R. McWhirter, A. Poff, M. Basavaraju, I. Rafi, E. Yemini, S. J. Cook, A. Abrams, B. Vidal, C. Cros, S. Tavazoie, N. Sestan, M. Hammarlund, O. Hobert, D. M. Miller 3rd, Molecular topography of an entire nervous system. *Cell* **184**, 4329–4347.e23 (2021).

63. C. M. Waterman-Storer, E. D. Salmon, Actomyosin-based retrograde flow of microtubules in the lamella of migrating epithelial cells influences microtubule dynamic instability and turnover and is associated with microtubule breakage and treadmilling. *J. Cell Biol.* **139**, 417–434 (1997).

64. T. Wu, J. J. Feng, A biomechanical model for fluidization of cells under dynamic strain. *Biophys. J.* **108**, 43–52 (2015).

65. M. Schenk, S. D. Guest, On zero stiffness. *Proc. Inst. Mech. Eng. C J. Mech. Eng. Sci.* **228**, 1701–1714 (2014).

66. M. B. Goodman, D. H. Hall, L. Avery, S. R. Lockery, Active currents regulate sensitivity and dynamic range in *C. elegans* neurons. *Neuron* **20**, 763–772 (1998).

67. J. G. White, E. Southgate, J. N. Thomson, S. Brenner, Touch-induced mechanical strain in somatosensory neurons is independent of extracellular matrix mutations in *Caenorhabditis elegans*. *Philos. Trans. R. Soc. Lond. B Biol. Sci.* **314**, 1–340 (1986).

68. T. B. Crapse, M. A. Sommer, Corollary discharge across the animal kingdom. *Nat. Rev. Neurosci.* **9**, 587–600 (2008).

69. H. Fehlauer, A. L. Nekimken, A. A. Kim, B. L. Pruitt, M. B. Goodman, M. Krieg, Using a microfluidics device for mechanical stimulation and high resolution imaging of *C. elegans*. *J. Vis. Exp.* **2018**, 56530 (2018).

70. T. Boothe, L. Hilbert, M. Heide, L. Berninger, W. B. Huttner, V. Zaburdaev, N. L. Vastenhouw, E. W. Myers, D. N. Drechsel, J. C. Rink, A tunable refractive index matching medium for live imaging cells, tissues and model organisms. *eLife* **6**, e27240 (2017).

71. A. L. Nekimken, B. L. Pruitt, M. B. Goodman, Touch-induced mechanical strain in somatosensory neurons is independent of extracellular matrix mutations in *Caenorhabditis elegans*. *Mol. Biol. Cell* **31**, 1735–1743 (2020).

72. M. Porta-de-la-Riva, L. Fontrodona, A. Villanueva, J. Cerón, Basic *Caenorhabditis elegans* methods: Synchronization and observation. *J. Vis. Exp.* e4019 (2012).

73. T. Stiernagle, in *WormBook: The Online Review of C. elegans Biology* (WormBook, 2006), pp. 1–11.

74. B. Sands, N. Burnaevskiy, S. R. Yun, M. M. Crane, M. Kaeberlein, A. Mendenhall, A toolkit for DNA assembly, genome engineering and multicolor imaging for *C. elegans*. *Transl. Med. Aging* **2**, 1–10 (2018).

75. A. Albeg, C. J. Smith, M. Chatzigeorgiou, D. G. Feitelson, D. H. Hall, W. R. Schafer, D. M. Miller III, M. Treinin, *C. elegans* multi-dendritic sensory neurons: Morphology and function. *Mol. Cell. Neurosci.* **46**, 308–317 (2011).

76. S. Redemann, S. Schloissnig, S. Ernst, A. Pozniakowsky, S. Ayloo, A. A. Hyman, H. Bringmann, Codon adaptation–based control of protein expression in *C. elegans*. *Nat. Methods* **8**, 250–252 (2011).

77. A. Paix, A. Folkmann, G. Seydoux, Precision genome editing using CRISPR-Cas9 and linear repair templates in *C. elegans*. *Methods* **121-122**, 86–93 (2017).

78. C. Frøkjær-Jensen, M. Wayne Davis, M. Sarov, J. Taylor, S. Flibotte, M. L. Bella, A. Pozniakovsky, D. G. Moerman, E. M. Jorgensen, Random and targeted transgene insertion in *Caenorhabditis elegans* using a modified *Mos1* transposon. *Nat. Methods* **11**, 529–534 (2014).

79. M. Harterink, P. van Bergeijk, C. Allier, B. de Haan, S. van den Heuvel, C. C. Hoogenraad, L. C. Kapitein, Light-controlled intracellular transport in *Caenorhabditis elegans*. *Curr. Biol.* **26**, R153–R154 (2016).

80. A. L. Nekimken, H. Fehlauer, A. A. Kim, S. N. Manosalvas-Kjono, P. Ladpli, F. Memon, D. Gopisetty, V. Sanchez, M. B. Goodman, B. L. Pruitt, M. Krieg, Pneumatic stimulation of *C. elegans* mechanoreceptor neurons in a microfluidic trap. *Lab Chip* **17**, 1116–1127 (2017).

81. J. H. Koschwanez, R. H. Carlson, D. R. Meldrum, Thin PDMS films using long spin times or tert-butyl alcohol as a solvent. *PLOS ONE* **4**, e4572 (2009).

82. A. Farré, F. Marsà, M. Montes-Usategui, Optimized back-focal-plane interferometry directly measures forces of optically trapped particles. *Opt. Express* **20**, 12270–12291 (2012).

83. J. Schindelin, I. Arganda-Carreras, E. Frise, V. Kaynig, M. Longair, T. Pietzsch, S. Preibisch, C. Rueden, S. Saalfeld, B. Schmid, J.-Y. Tinevez, D. J. White, V. Hartenstein, K. Eliceiri, P. Tomancak, A. Cardona, Fiji: An open-source platform for biological-image analysis. *Nat. Methods* **9**, 676–682 (2012).

84. K. C. Johnson, W. E. Thomas, How do we know when single-molecule force spectroscopy really tests single bonds? *Biophys. J.* **114**, 2032–2039 (2018).

85. T. Duong, ks: Kernel density estimation and kernel discriminant analysis for multivariate data in R. *J. Stat. Softw.* **21**, 1–16 (2007).

86. J. Chacon, T. Duong, *Monograps on Statistics and Applied Probability 160: Multivariate Kernel Smoothing and its Application* (Taylor & Francis, 2018).

87. J. Ho, T. Tumkaya, S. Aryal, H. Choi, A. Claridge-Chang, Moving beyond *P* values: Data analysis with estimation graphics. *Nat. Methods* **16**, 565–566 (2019).

88. A. Nekouzadeh, Y. Rudy, Statistical properties of ion channel records. Part II: Estimation from the macroscopic current. *Math. Biosci.* **210**, 315–334 (2007).

89. E. A. Evans, D. A. Calderwood, Forces and bond dynamics in cell adhesion. *Science* **316**, 1148–1153 (2007).

90. S. Bechstedt, J. Howard, in *Current Topics in Membranes* (Elsevier, 2007), vol. 59, pp. 399–424.

91. Z. Yan, W. Zhang, Y. He, D. Gorczyca, Y. Xiang, L. E. Cheng, S. Meltzer, L. Y. Jan, Y. N. Jan, *Drosophila* NOMPC is a mechanotransduction channel subunit for gentle-touch sensation. *Nature* **493**, 221–225 (2013).

92. J. T. Brennecke, B. L. de Groot, Mechanism of mechanosensitive gating of the TREK-2 potassium channel. *Biophys. J.* **114**, 1336–1343 (2018).

93. M. Harterink, S. L. Edwards, B. de Haan, K. W. Yau, S. van den Heuvel, L. C. Kapitein, K. G. Miller, C. C. Hoogenraad, Local microtubule organization promotes cargo transport in *C. elegans* dendrites. *J. Cell Sci.* **131**, jcs223107 (2018).

Citation: R. Das, L.-C. Lin, F. Català-Castro, N. Malaiwong, N. Sanfeliu-Cerdán, M. Porta-de-la-Riva, A. Pidde, M. Krieg, An asymmetric mechanical code ciphers curvature-dependent proprioceptor activity. *Sci. Adv.* **7**, eabg4617 (2021).